The influence of swash-based reflection on surf zone hydrodynamics: a wave-by-wave approach

Kévin Martins, Chris E Blenkinsopp, Rafael Almar, Jun Zang

Coastal Engineering 122 (2017) 27–43

Contents lists available at ScienceDirect

Coastal Engineering

journal homepage: www.elsevier.com/locate/coastaleng

The influence of swash-based reflection on surf zone hydrodynamics: a wave-by-wave approach

Kévin Martins[a,*], Chris E. Blenkinsopp[a], Rafael Almar[b], Jun Zang[a]

[a] Research Unit for Water, Environment and Infrastructure Resilience (WEIR), Department of Architecture and Civil Engineering, University of Bath, Claverton Down Road, Bath BA2 7AY, UK

[b] LEGOS (CNRS/CNES/IRD/Université de Toulouse), Toulouse, France

ARTICLE INFO

Keywords:
CFD
OpenFOAM®
Surf zone
Prototype laboratory experiments
Swash-based reflection
Radon transform
Wave-by-wave approach

ABSTRACT

A detailed understanding of the behaviour of waves in the nearshore is essential for coastal engineers as these waves cause beach erosion, coastal flooding and damage to coastal structures. Significantly, the influence of reflected waves is often neglected in surf zone studies, although they are known to influence wave properties and circulation in the nearshore. In this paper, a phase-resolving model is rigorously applied to model conditions from the prototype-scale BARDEXII experiment in order to examine and assess the influence of swash-based reflection on surf zone hydrodynamics at both the individual wave and time-averaged timescales. Surface elevation is separated into incoming and outgoing signals using the Radon Transform and a crest tracking algorithm is used to extract incident and reflected wave properties. It is found that on steep beaches ($\tan\beta > 1{:}\,9$) the swash-based reflection - the reflection generated in the swash during the backwash - contributes significantly to the intrawave variability of individual wave properties such as the wave height to water depth ratio γ, through the generation of quasi-nodes/antinodes system. For γ expressed with individual wave heights, variations up to 25% and 40% are obtained for the modelled regular and irregular wave tests, whereas it reaches 15% when it is based on the significant wave height. The outgoing wave field-induced hydrodynamics is also found to affect time-averaged parameters: undertow and horizontal velocity skewness. The undertow is mainly strengthened, particularly in the shoaling region where the outgoing component dominates over the contribution from the incoming wave field. Offshore of the bar, an onshore-directed flow streaming close to the bed is also generated under the outgoing wave field, and is suspected to help in stabilising the bar position. This, along with the influence of the outgoing wave field on the horizontal velocity skewness and the presence of quasi-standing waves, suggests a complex contribution of the hydrodynamics induced by swash-based reflection into sediment transport rates and nearshore bar generation/migration.

1. Introduction

Wave reflection from beaches and other coastal features is known to influence incident wave-induced hydrodynamics and therefore morphodynamics [12].

While there are many studies of structure-induced reflection present in the literature (see Zanuttigh and van der Meer [3], for a relatively recent comparison of extensive datasets), it is evident that prior studies focusing on wave reflection from natural beaches, especially in the sea/swell band ($0.05\ \text{Hz} \leq f \leq 0.5\ \text{Hz}$), are relatively limited. The reflection of monochromatic waves over a slope was first investigated by Iribarren and Nogales [4], and Miche [5] and it has been shown that the reflection coefficient of a slope, defined as the ratio between incident and reflected wave height $K = H_r/H_i$, is linked to the surf-similarity parameter [6]:

$$\xi = \tan\beta/\sqrt{H_o/L_o} \tag{1}$$

where β is the structure or beach slope, and H_o and L_o are the offshore wave height and wavelength, respectively. While the reflected wave phase was found to be only dependent on the offshore wave steepness and the slope [7], the amplitude of reflected waves are substantially influenced by the bottom roughness and permeability, but also the nature of wave transformation across the surf zone (Battjes [6], Hughes and Fowler [7], Miles and Russell [8] and many others). By presenting cross-shore varying reflection coefficients from two field-based experimental datasets, Baquerizo et al. [9] observed a net increase in reflection coefficients shoreward of the break point, and suggested that when defining the reflection coefficient of a beach, it should be

* Corresponding author.
E-mail addresses: K.Martins@bath.ac.uk (K. Martins), C.Blenkinsopp@bath.ac.uk (C.E. Blenkinsopp), rafael.almar@ird.fr (R. Almar), j.zang@bath.ac.uk (J. Zang).

http://dx.doi.org/10.1016/j.coastaleng.2017.01.006
Received 21 June 2016; Received in revised form 22 December 2016; Accepted 27 January 2017
Available online 14 February 2017

measured as far offshore as possible. Although this approach is appropriate for studying the bulk outgoing wave energy from a beach, it presents several issues. Assessing the outgoing energy further from shore increases the risk of observing additional phenomenon, particularly from non-linear wave interactions [10,11], that can lead to reflection coefficients higher than unity [12]. Furthermore and as discussed by Battjes [6], based on the methodology of Miche [5], the processes responsible for incident wave energy dissipation in the surf zone (mainly friction and breaking) have to be approximated, while a measurement close to the swash zone would lead to an exact estimation of reflected waves (height and phase), using the local incident properties.

In the few field-based studies focusing on wave reflection in the sea/swell range of frequencies, it was generally demonstrated that reflection could be substantial [13,8,14]. Using an array of 24 bottom-mounted pressure sensors, Elgar et al. [13] found that up to 18% of the incident sea-swell frequency band was reflected back into the surf zone. These relatively high levels of reflected energy in the surf affect the incident waves in a variety of ways. Fluctuations in the currents velocities due to the reflected wave orbital velocities influence the sediment suspension [1], also potentially influencing the velocity skewness, important for onshore sediment transport [15,16]. Instantaneous sea levels are also influenced by the presence of seaward propagating wave crests and troughs, which influence the wave height to depth ratio γ, due to the presence of quasi-standing waves [17]. Many parameterisations are present in the literature to describe the cross-shore variation of this wave parameter, related to the wave energy dissipation (see for example the pioneering work of Battjes and Janssen [18]). While existing parameterisations of γ do not explicitly account for wave reflection, both γ and reflection are a function of beach slope and wave number [19,20,21]. It is known that the beach slope controls the wave reflection to a great extent (see above, and Almar et al. [14,22]). Through observation of the influence of strong backwash flows on the generation of individual reflected waves at the surf-swash boundary, a link might be expected between reflected waves generated by swash flows and the wave height to water depth ratio of individual waves in the surf zone, though no evidence is present in the literature.

A lack of field-based studies of sea/swell reflection on beaches can be explained by the complexity in measuring the energy bulk reflected from a beachface. Several methods to separate incoming from outgoing wave fields exist; see for example Inch et al. [23] for a recent description. Correlation functions between 2 wave gauges were used (Kajima [24], Thornton and Calhoun [25] in Goda and Suzuki [26]) before Goda and Suzuki [26] introduced the use of Fast-Fourier Transform (FFT) to speed up this process. This was later extended to a larger array of wave gauges - see for example Mansard and Funke [27], Zelt and Skjelbreia [28] or Lin and Huang [29] - which enables the error in the separation process to be reduced [23]. Other methods such as PUV (Pressure, U horizontal and V vertical current velocities, Guza and Bowen [30]), or approaches based on long-wave theory described in Guza et al. [31] use collocated pressure or surface elevation signals, and horizontal current velocities to separate incoming and outgoing signals at a cross-shore location. Using a totally different approach, Almar et al. [32] describe the use of the Radon Transform (RT) for nearshore wave studies, with the objective of finding tools to facilitate wave-by-wave analyses. Mostly used in image processing, the RT can be applied to the projection of a cross-shore/temporal diagram $\eta(x, t)$ into points in the Radon (polar) space. This method is therefore particularly suitable in the surf zone as with increasing non-linearities, the wave tracks appear as well-defined lines in such diagrams (e.g. Almar et al. [33]). Almar et al. [32] successfully separated incident and reflected long-wave signals from a laboratory dataset and demonstrated that the results compared well with those from a Boussinesq model.

In this study, the RT is applied to the results from a phase-resolving numerical model simulating two monochromatic and one irregular wave tests, performed at prototype-scale in the Delta flume during the BARDEXII project [34]. The primary objective is to study the impact of reflected waves on incident wave properties and surf hydrodynamics with a focus on sea/swell waves. For irregular waves, the free surface is actually a sum of wave trains, with different frequency and possibly direction (incident and reflected). In this regard, a wave-by-wave approach is developed based on the previous work of Martins et al. [21], allowing individual wave tracking from the shoaling area to the runup limit, and back into the flume after reflection.

The paper is organised as follows. Section 2 introduces the experimental and numerical datasets. The numerical model is validated using a large array of instruments, including a Terrestrial Laser Scanner (TLS) that enables the description of the wave shape during breaking. The signal separation in incoming/outgoing components and the wave-by-wave approach used to track individual wave properties are described in Section 3. Section 4 presents the results on the separation methods and its application for the study of swash-based reflection influence on surf zone hydrodynamics at the individual wave timescale. The concept of swash-based reflection is notably explained through a link with swash events potential energy. The results and the influence of reflection at longer timescales are then discussed in Section 5. Finally Section 6 provides the conclusions of this study.

2. Experimental and numerical datasets

2.1. The BARDEXII experiments

The present study uses experimental data obtained during the 2-month-long BARDEXII experiment [34]. In order to study wave processes and cross-shore sediment transport in the surf and swash zones, a coarse sandy beach/barrier system was built in the prototype-scale Delta Flume (Vollenhove, The Netherlands). The A6 and A7 monochromatic test cases (hereafter A6-mono and A7-mono) and A6-01 irregular wave test are the focus of the present study [34]. Regular second-order Stokes waves were generated during the A6-mono and A7-mono tests by a second-order wave steering system at x=0 m, with an Active Reflection Compensation system (ARC) for the absorption of reflected waves. For the A6-01 irregular test, a JONSWAP spectrum with a peak enhancement factor of 3.3, was imposed in the wave flume. The initial beach profile of 1:15 slope between $x = 49 - 109$ m evolved under the wave action during Series A1 to A7 to result in the bed profiles presented in Fig. 1, presenting a much steeper upper beach face, a bar system for the A6-01 and A6-mono, and a terrace for the A7-mono. The wave forcing conditions and beach slope for the different wave tests examined here are presented in Table 1.

A large array of instrumentation was used during the experiments, and only part of the experimental dataset is used to validate the numerical model used herein. The positions of the instruments used in the present work are shown in Fig. 1. A series of pressure transducers (PT) and electro-magnetic current meters (EMCM) both sampled at 20 Hz were located in the shoaling and surf zones to measure the pressure and flow velocity under propagating and breaking waves. Two terrestrial laser scanners were deployed to measure free surface elevations within the flume, the first was positioned in the surf zone at x=73.6 m, 3.9 m above mean sea level (MSL) while the second was deployed at x=88.3 m, 3.8 m above MSL to study the swash zone hydrodynamics and morphodynamics. The TLS recorded data at an angular resolution of 0.25° and sample rate of 35 Hz; the measurements were processed following Martins et al. [21] including the correction of the scanner orientation, noise filtering and spatial interpolation onto a regular grid.

TLS data is ideal for wave-by-wave analysis of surf zone processes as the high-spatial and temporal resolutions of the measurements allow for the description of wave geometry and the tracking of individual wave properties through hundreds of cross-shore positions. Physical

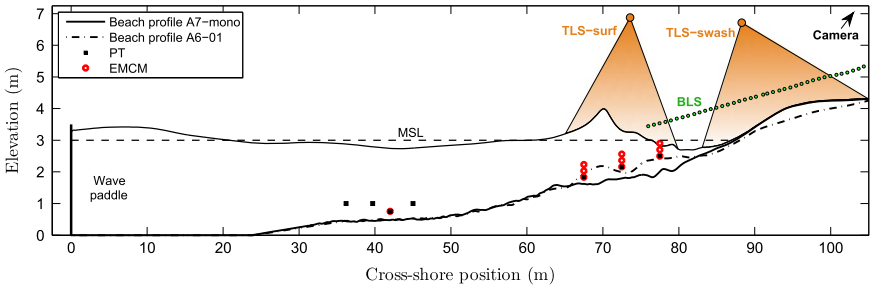

Fig. 1. Schematic of the experimental setup for the A6-mono, A7-mono and A6-01 wave tests. The two different initial beach profiles are shown. A dataset from the following instruments was used in the present study: 7 pressure transducers (PT) and electro-magnetic current meters (EMCM) located in the shoaling and surf zones and two terrestrial laser scanners (TLS) deployed at 6.8 and 6.9 m above the flume bed (3.8 and 3.9 mMSL, respectively) within the surf and swash zones. The zones covered by the TLS are indicated with the orange cones.

Table 1
Wave and beach conditions for the different wave tests. For the monochromatic wave tests, H_o was computed as four times the standard deviation of the surface elevation measured at the wave paddle.

Run	H_o (m)	T_p (s)	MSL (m)	β_{surf}	β_{swash}	ξ_{surf}	ξ_{swash}
A1-mono	0.94	8	3.00	1:13	1:11	0.52	0.60
A2-mono	0.71	8	3.00	1:13	1:13	0.58	0.61
A4-mono	0.67	8	3.00	1:14	1:10	0.58	0.83
A6-01	0.70	10.90	2.98	1:12	1:9	0.63	0.97
A6-mono	0.74	12.10	3.00	1:15	1:8	0.64	1.10
A7-mono	0.76	12.10	3.00	1:17	1:8	0.54	1.18
A7T10-mono	–	10	3.00	1:17	1:8	0.49	1.07
A7T11-mono	–	11	3.00	1:17	1:8	0.52	1.12

constraints within the flume limited the elevation of the TLS and hence the horizontal extent of the measurements, however the high resolution of the data enabled the wave shape to be captured in the swash zone and around the primary break point for detailed model validation.

The PT data were used to retrieve the surface elevation using the linear wave theory, and the classic pressure response factor (see e.g. Bishop and Donelan [35]):

$$K_p = \frac{\cosh(k(\bar{h} + z))}{\cosh(k\bar{h})} \tag{2}$$

where $\bar{h}$ is the mean water depth, k is the radian wavenumber and z the PT deployment depth. The methodology described by Inch [36] was followed, using the high frequency cut-off $w_c = 0.564\pi\sqrt{g/\bar{h}}$ (where g is gravity) proposed in Green [37], to prevent noise amplification. Correcting the signal depth attenuation with linear wave theory is known to lead to an underestimation of the wave crest elevation, especially for highly non-linear waves, see for instance Nielsen [38], Townsend and Fenton [39] or Barker and Sobey [40]. Bishop and Donelan [35] suggested that wave heights could be retrieved within 5%, but no estimation based on wave-by-wave analysis has ever been carried out, thus the impact of the correction at this time scale is unknown. For that reason, the differences at the wave-by-wave scale between the TLS and PT datasets were assessed prior to any model validation.

Fig. 2a shows the wave profiles measured at x=72.5 m, close to the break point, by both instruments for every wave of the A7-mono test case and its ensemble-average, with the modelled surface elevation also shown. In this study, the break point is defined as the point of maximum wave height; for this comparison it was assessed from the wave height evolution (TLS), comparisons between model and data presented further in this paper, and from video data (not shown here) in order to exclude the presence of foam that could increase discrepancies between datasets. It is demonstrated that at the early stage of breaking, the individual wave height is underestimated by approximately 30%. Additionally, considerable differences are observed in the two wave shapes (skewness and steepness): wave non-linearities at the wave-by-wave scale are largely underestimated when using the linear theory to retrieve the surface elevation. For these reasons, the raw pressure signals along the wave flume were used to validate the model. Fig. 2b shows the ratio of the measured raw pressure to hydrostatic pressure, based on the surface elevation measured by the TLS. It is observed that the two estimates differ significantly before the wave crest where the pressure is higher than hydrostatic and at the crest location, where the measured pressure is well below hydrostatic; a result consistent with previous experimental datasets [41].

Closer to shore, an array of 45 ultrasonic bed level sensors (BLS, see Fig. 1 for locations) were deployed in the swash zone to measure water depths and monitor high-frequency bed level changes [42]. Sampling at 4 Hz, the BLS are able to measure water depths and bed-level changes using acoustic signals with an accuracy of the order of 1 millimetre. Finally, an ARGUS video camera system was deployed above the beach, in order to monitor surf, swash and overwash processes. In this study, timestacks from the swash camera were used to track the instantaneous shoreline position for comparison with the simulated results.

2.2. Numerical model: IHFOAM [43]

The IHFOAM model [43], based on the CFD package OpenFOAM® (v2.1.1 in the present study) was used to generate waves and simulate their propagation across the wave flume. A library for the wave generation and absorption at boundaries was implemented and the solver modified accordingly. The RANS equations described in Higuera et al. [43] are solved using a VOF (Volume-of-Fluid) method to describe and track the free surface. A rectangular 2D computational mesh for each run was constructed based on survey data, using a cross-shore spacing of dx=0.05 cm and a varying dz, corresponding to a grid of 2100 × 60 = 126000 cells. The 2D mesh was manually created using the '.msh' format based on the window-averaged profile, so that no abrupt changes occur near the bed (see Fig. 3a). It was then transformed into the OpenFOAM format using the *gmshtofoam* built-in function. The number of vertical layers was chosen such that the cell aspect ratio was approximately unity near the breaking zone (Fig. 3b) to more accurately resolve the break point [44]. Sensitivity testing enabled the mesh size to be optimised to obtain a good compromise between CPU time and precision. A desktop PC with 8 Gb of RAM and a 3.20 GHz quad-core processor was used to run the simulation, with a typical time step of 0.0005 s, varying to fulfil the CourantFriedrichsLewy (CFL) local restrictions. For an 80 second run, this corresponded to approximately 53 h of CPU time.

Boundary conditions at the wave paddle were generated using second-order Stokes theory [45] for the A6 and A7 monochromatic wave cases. The A6-01 irregular wave case was generated using the actual wavemaker signal (paddle displacement and surface elevation). The active absorption at the wave paddle (located at x=0, see Fig. 1) was activated as the Delta flume is equipped with an ARC system, preventing radiated components from being re-reflected towards the

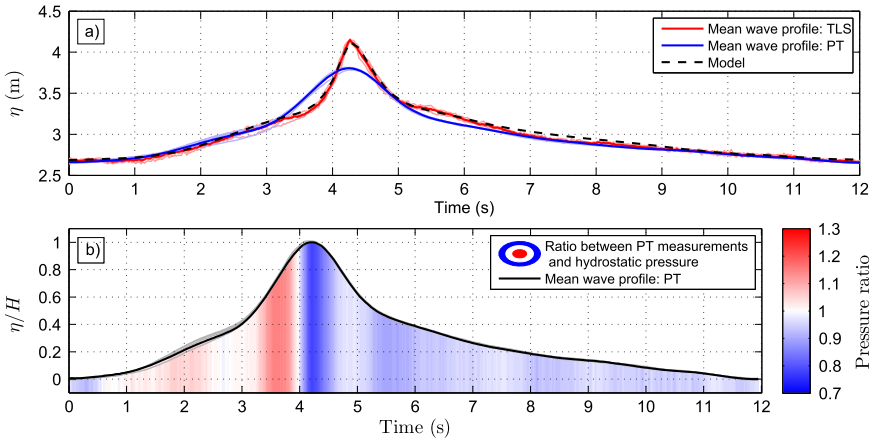

Fig. 2. Comparison of individual wave profiles obtained from the surf-zone TLS and the PT, at the PT location x = 72.5 m for the A7-mono test. Panel a) shows the wave profile of the modelled waves (light red and blue lines for the TLS and PT, respectively) with the ensemble averaged (thick red and blue lines for the TLS and PT, respectively). The modelled wave profile at that location is also shown as dashed black-line. In panel b), a contour plot of the ratio between the raw measured pressure and hydrostatic pressure based on the surface elevation measured by the TLS is shown: red zones correspond to periods when the pressure is higher than the hydrostatic, and blue zones correspond to periods where it is lower. The ensemble-averaged wave profile is shown as black line, while the gray lines represent individual wave profiles measured by the PT. (For interpretation of the references to color in this figure legend, the reader is referred to the web version of this article.)

artificial beach.

The VOF-based CFD method attributes an α value to the typically two modelled phases of interest, for instance air and water [46]. A cell containing only water corresponds to $\alpha = 1$, whereas a cell filled with air corresponds to $\alpha = 0$. The free surface was extracted by integrating α over the water column at a given position. This method is considered particularly suitable for spilling or weakly plunging waves, characterized by relatively low air entrainment. Finally, the $k - \omega$ SST turbulence closure model developed by Menter [47] was used as it as found to better reproduce the surface elevation than the classical $k - \epsilon$ and $k - \omega$ models [48]. For further details on the model equations, the reader is referred to Higuera et al. [43].

2.3. Validation of the numerical model

2.3.1. Surface elevation and relative pressure in the surf zone

The detailed surface elevation measurements from the TLS and ultrasonic BLS were used to validate the model predictions of free surface elevation around the break point. Fig. 4 shows instantaneous comparisons between the TLS and BLS measurements and the modelled water phase for the A7-mono test case at 6 times during the breaking process. Comparisons show good agreement (RSME <0.06 m, $r^2 > 0.96$) at every stage of the breaking (wave shape evolution and breaking location), with the modelled free surface closely capturing the complex wave geometry resolved from hundreds of point measurements obtained by the TLS. Despite this good model agreement in mean errors (Table 2), the existence of short duration, low void fraction, but large magnitude splashes generated during breaking (landward of x=76 m, see Fig. 4d) lead to large maximum errors (MAE). These splashes are captured by the TLS once the wave crest propagates landward of x=76 m but are not expected to be resolved by the CFD model. In opposition, the significant MAE observed for the PT (Table 2) are due to the poor performance of linear theory to retrieve the surface elevation a this location (Fig. 2).

To validate the modelled wave transformation across the wave flume the modelled relative pressure was compared with the raw pressure data from the PTs. For conciseness, only results for the 670 s-long A6-01 irregular wave test are shown; the statistical errors from all tests are shown in Table 2. Fig. 5 shows a 360 second window of the modelled and measured relative pressure timeseries from the shoaling area to the surf zone. The transformation of the incident waves is well described by the model (RMSE =0.02 – 0.04 dbar and $r^2 = 0.92 - 0.97$), with a good representation of the wave profile changes. Though it is less clear than from a surface elevation timeseries, the more tooth-shaped wave profile after breaking (from x=72.5 m) can clearly be seen. These comparisons show the potential of using the piston-type boundary conditions to generate irregular wave trains in prototype-scale experiments.

2.3.2. Surf and the swash hydrodynamics

Horizontal and vertical current velocities were measured at various cross-shore locations along the wave flume (see Fig. 1). These

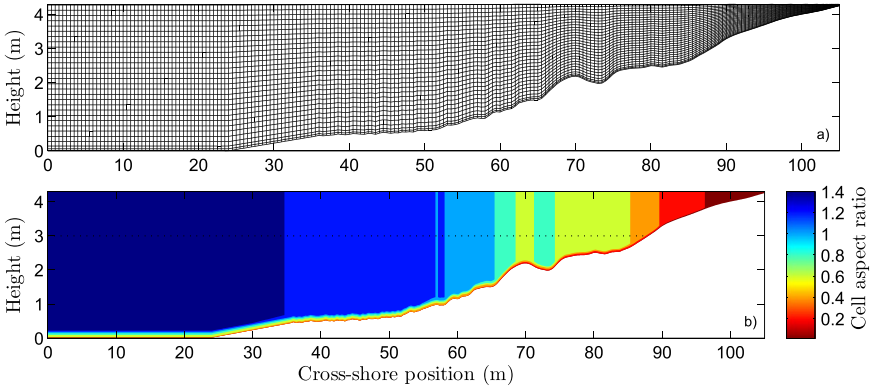

Fig. 3. Description of the computational mesh: a) rectangle-based computational mesh for the A6-01 wave test, for visual reasons only every 2nd cell in the vertical direction and 10th cell in the horizontal direction are shown; b) contour plot of the cell aspect ratio. (For interpretation of the references to color in this figure legend, the reader is referred to the web version of this article.)

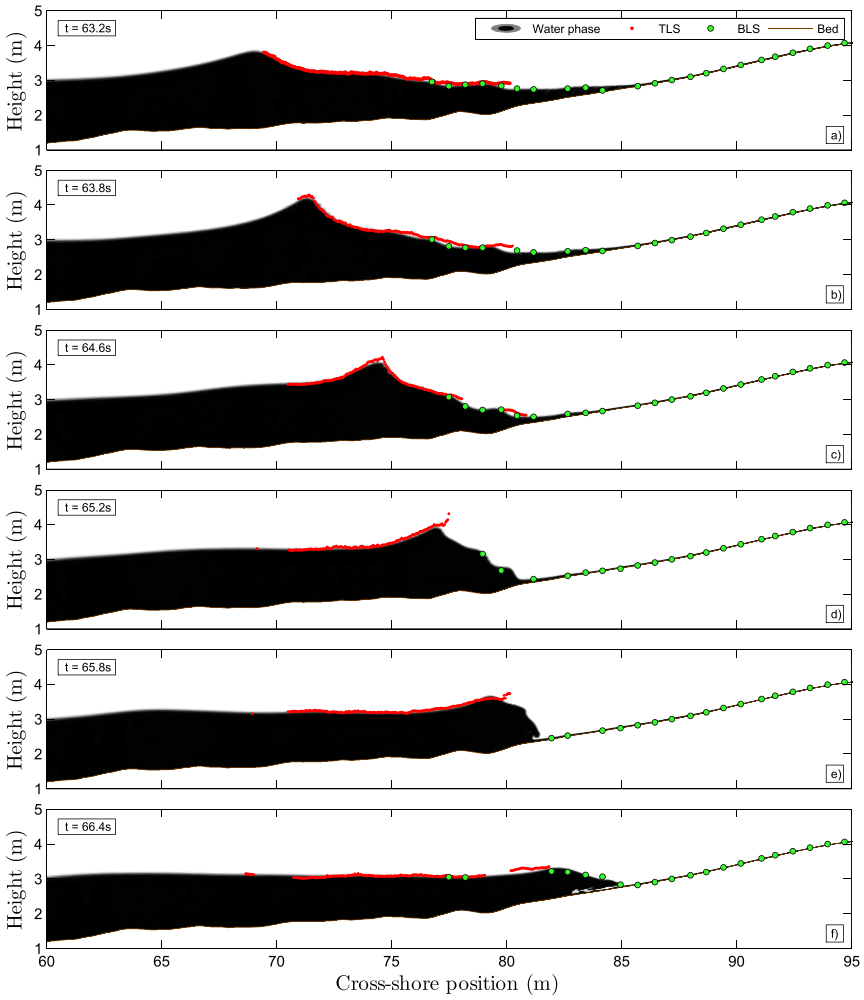

Fig. 4. Comparison of the modelled water phase from the A7-mono wave test with the instantaneous free-surface elevation measurements from the TLS and the ultrasonic BLS. Six moments of the breaking process are shown.

measurements were used to validate the modelled wave-induced hydrodynamics in the shoaling and surf zones. Fig. 6 shows comparisons of measured and modelled horizontal and vertical velocities for the A6-01 irregular wave test. Overall, the model successfully reproduces the wave-induced hydrodynamics through the shoaling region and surf zone (similar good agreement was found for the regular wave tests, see Table 2). More specifically, the high-magnitude current velocities observed after breaking (x=77.5 m) are well described in the numerical model. Some discrepancies are observed in these comparisons, where measured current velocities are noisy in some locations, e.g. close to the surface at x=77.5 m and z=2.70 m. These periods occur during the passage of the two largest wave groups, and could be explained by a high concentration of entrained air bubbles, which are known to introduce noise when using EMCMs (see for example Gailani and Smith [49], Elgar et al. [50] or Huang and Hwang [51]).

As the swash zone is thought to significantly influence surf zone processes [2], primarily due to its role in reflecting incident wave energy, the ability of the model to reproduce swash zone processes was assessed. The model results were compared against measurements of the shoreline position (ARGUS video camera) and swash depths (BLS and TLS). The cross-shore position of the shoreline was manually extracted from the video timestacks. The modelled shoreline was computed using a 3 cm threshold from the modelled water depths. Both modelled and measured shoreline cross-shore positions were transformed into a vertical elevation using the surveyed beach profile. Fig. 7 shows the timeseries comparisons of modelled and measured shoreline elevation for the entire A6-01 test, along with a 2-minute subset of the data comparing cross-shore shoreline position and swash depths. Although the modelled runup extent is sometimes slightly overestimated (Fig. 7a and b), comparisons show very good agreements between the two datasets. In particular, the timing of the uprush and downrush phases (Fig. 7b) as well as water volumes (Fig. 7c-e) are accurately reproduced. Figs. 7c-e highlight some pros and cons of different methods for measuring flow depths in the swash zone (TLS and ultrasonic BLS in this case). In Fig. 7d, it is observed that there are periods, particularly in the lower swash during backwash where insufficient light is scattered by the water surface and no signal return is detected by the TLS. Reduced ability to detect water depths during backwash and close to the shoreline is common when using TLS, and enhanced here by the reduced persistence of aeration observed in freshwater (e.g. Blenkinsopp and Chaplin [52]). This effect means that TLS measurements tend to underestimate the shoreline position as observed by [53]. By contrast, the measurements from the BLS are much more consistent but are limited by the much reduced spatial resolution, meaning that the wave/bore front is less well resolved.

3. Methods

3.1. Separation of the incoming and outgoing signals

In the present study, the influence of reflected waves was studied at

Table 2
Model skill for reproducing η (PT and TLS), p (PT), u and v (EMCM): root-mean square error (RMSE), absolute mean error, maximum absolute error and r the linear correlation coefficient (defined as the ratio between the covariance of the two timeseries, and the product of their standard deviation). For conciseness, only minimum and maximum values along the flume are shown, for every modelled quantity and wave test. For the TLS, statistics are calculated only between $x = 70 - 78$ m, whereas for the PT, it concerns the PT positions visible in Fig. 1.

Quantity	Run	RMSE	AME	MAE	r^2
	A6-mono	0.05–0.08 m	0.04–0.06 m	0.12–0.45 m	0.84–0.98
$PT - \eta$	A7-mono	0.04–0.06 m	0.03–0.04 m	0.12–0.32 m	0.93–0.98
	A6-01	0.03–0.06 m	0.02–0.04 m	0.15–0.45 m	0.85–0.97
	A6-mono	0.04–0.08 m	0.04–0.06 m	0.10–0.6 m	0.95–0.99
$TLS - \eta$	A7-mono	0.03–0.06 m	0.02–0.04 m	0.09–0.6 m	0.96–0.99
	A6-01	0.06–0.08 m	0.04–0.06 m	0.6–0.8 m	0.85–0.90
	A6-mono	0.02–0.04 dbar	0.02–0.03 dbar	0.06–0.11 dbar	0.98–0.99
p	A7-mono	0.02–0.03 dbar	0.01–0.02 dbar	0.06–0.11 dbar	0.99
	A6-01	0.02–0.04 dbar	0.02–0.03 dbar	0.10–0.24 dbar	0.92–0.97
	A6-mono	0.06–0.15 m/s	0.05–0.10 m/s	0.18–0.55 m/s	0.89–0.98
u	A7-mono	0.04–0.20 m/s	0.03–0.17 m/s	0.11–0.47 m/s	0.97–0.98
	A6-01	0.06–0.27 m/s	0.05–0.20 m/s	0.25–1.90 m/s	0.78–0.96
	A6-mono	0.02–0.09 m/s	0.02–0.07 m/s	0.12–0.32 m/s	0.38–0.70
v	A7-mono	0.02–0.09 m/s	0.02–0.07 m/s	0.06–0.32 m/s	0.47–0.84
	A6-01	0.02–0.12 m/s	0.01–0.07 m/s	0.17–1.52 m/s	0.19–0.21

two distinct timescales: individual wave timescale and time-averaged over a complete wave test. In order to study the evolution of individual incident wave properties, the Radon Transform (RT) was applied to the modelled free surface elevation to separate the incoming and outgoing signals. The RT was successfully applied to study wave celerity and incident and reflected short and long waves by Almar et al. [33] and Almar et al. [32]. The method applies the following transformation [54] to a surface elevation signal $\eta(x, t)$:

$$R(\rho, \theta) = \iint \eta(x, t)\delta(x\cos\theta + t\sin\theta - \rho)dxdt \quad (3)$$

where x represents the cross-shore dimension, and t is time, δ is the Dirac function, ρ and θ the distance and angle from origin of the integration line defined by $\rho = x\cos\theta + t\sin\theta$ [32]. As described in Almar et al. [32], lines in the Cartesian spatio-temporal space ($\eta(x, t)$ diagram) are represented by points in the Radon space.

More interestingly for the present study, when a wave reflects off the beach, it is also visible as a line in the aforementioned $\eta(x, t)$ diagram. By integrating the Radon signal over the correct angles with the inverse RT [32], the separation of the incoming and outgoing signals is made possible. The result enables the modelled surface elevation to be described as:

$$\eta(x, t) = \eta_{inc}(x, t) + \eta_{out}(x, t) \quad (4)$$

where the '*inc*' and '*out*' subscripts refer to the incoming and outgoing components respectively. An example of this process is shown in Fig. 8 for the A7-mono test which demonstrates the strength of this method: incident (Fig. 8b) and reflected waves (Fig. 8c) clearly appear as lines in the $\eta(x, t)$ diagram. Note that in this study, a difference is made between 'reflected' wave and 'outgoing' signal. While at the wave-by-wave time scale it is evident that the wave propagating seaward from the beach upper slope is generated through reflection, it is not clear how other signals propagating seaward are originated, especially at longer time scales (e.g. non-linear interactions). The term 'reflected wave' is therefore only used to describe seaward propagating waves generated at the boundary between the swash backwash and the inner surf that can be tracked (swash-based reflection). The same reasoning is applied to differentiate 'incident' wave from 'incoming' signal.

The separation based on the RT was compared in the frequency domain to the commonly used method of Guza et al. [31] (hereafter Guza84). The Guza84 method was developed from long-wave theory and uses collocated surface elevation and horizontal current velocities signals to separate the incoming and outgoing components of surface elevation or horizontal current velocities. The use of this linear theory-based method is motivated by two reasons: 1) a performance comparison with the RT to assess the model capacity in reproducing the wave spectra and 2) the observed poor performance of the RT to resolve mean flow velocities after separation. While the RT was found to satisfactorily separate incoming and outgoing signals (for both η and u), mean incoming and outgoing cross-shore flow velocities close to zero were found when time-averaged. The two possible explanations are the introduction of noise in the high frequencies, which makes the average of the whole signal tend to zero, or the less sharp 'lines' in the $u(x, t)$ diagram, compared to the $\eta(x, t)$ diagram observable in Fig. 8a.

For this reason, linear theory was used to separate surface elevation and horizontal current velocity in order to study the influence of reflection on time-averaged surf zone parameters (undertow, wave setup and horizontal velocity skewness). Modelled horizontal current velocities were extracted from the results of the A6-01 test along the wave flume at various heights above the bed ranging from 0.01 m to 1.8 m (non-dimensional height $z' = z/\bar{h} \in [0, 0.6]$) using the Guza84 method [55]. After performing the aforementioned current separation, horizontal current velocities were averaged over the entire test to compute the mean cross-shore current velocities (undertow) and velocity skewness defined as $S_k = \overline{u^3}/\overline{u^2}^{3/2}$, where $\overline{.}$ is the time-averaging operator.

3.2. Wave-by-wave approach

The results at the individual wave timescale presented in this paper rely on a wave-by-wave analysis, performed separately on the extracted incoming and outgoing signals. At every cross-shore position between x=0 and 84 m, local peaks in the surface elevation timeseries (corresponding to wave crests) are identified to enable the extraction of individual wave properties (e.g. H,T), following an improved version of the methodology presented in Martins et al. [21]. Previous work has been undertaken to study individual wave properties; see for example recent studies of Power et al. [56,57], Postacchini and Brocchini [58]. These methods are based on peak-to-peak analysis which bypasses the need for low-pass filtering but cannot deal with the superposition of waves travelling in either the same or opposing directions.

The present algorithm starts by extracting wave properties at an initial cross-shore position (e.g. x=0 m, for incident waves) using peak analysis: wave crests are detected and wave troughs are defined as the minimum reached between two crests. Wave height H is then defined as the height difference between crest and trough levels, and the wave period T corresponds to the time between the two troughs surrounding this wave crest. From this initial position, every detected wave (or a manually-selected subset) can be tracked. At each new cross-shore position, the time of wave crest detection at the previous cross-shore position is compared to the detection time at the new location. If a wave crest is detected within a reasonable physical range (based on wave celerity), it is kept as the new position. If no value is found, wave tracking is ceased. The same methodology can be applied to both incoming and outgoing signals, with the values for the physical range set accordingly. The result of this wave tracking algorithm on the A7-mono test is shown in Fig. 8.

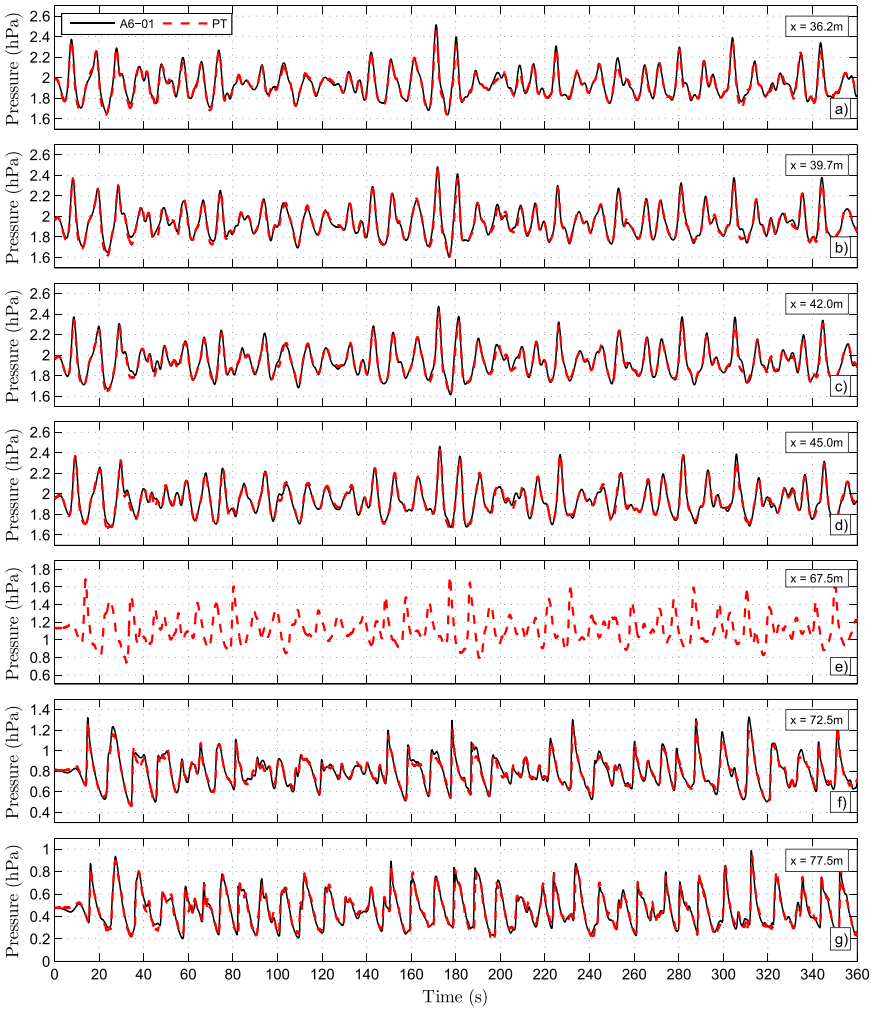

Fig. 5. Validation of the modelled relative pressure at the PT locations for the A6-01 wave test, for the first 320 s of the simulation. The model and data timeseries are shown at five locations in the shoaling region and two in the surf zone. As seen in Fig. 1, the pressure sensor located at x = 67.5 m is slightly buried, the model therefore cannot provide any signal for this location (out of domain).

Using two separate analyses, this methodology was performed on the total $\eta(x, t)$ and incoming $\eta_{inc}(x, t)$ signals. The following individual wave properties were extracted: crest height C, wave height H, period T, and depth under preceding trough h_{tr}. The analysis performed on the incoming signal allows for the retrieval of incident wave properties, by removing the effect/component of reflected waves from the total signal. Reflected wave properties were also extracted from the outgoing $\eta_{out}(x, t)$ signal in order to assess the incoming/outgoing energy ratio and study their characteristics as a function of the incident wave properties.

4. Results

4.1. Inter-comparison of separation methods

Model and experimental data from the A6-01 irregular wave test were compared in the frequency domain by applying the RT on the modelled free surface elevation and the Guza84 method on the collocated PT/EMCM data. Fig. 9 shows the comparison of the total, incoming and outgoing signals at four cross-shore locations: x=42, 67.5, 72.5 and 77.5 m. At all positions, and for both sea-swell and infragravity ranges of frequencies, the comparisons show good agreement. Although the amount of energy is small, more incoming energy at the infragravity frequencies (0.005 Hz $\leq f \leq$ 0.05 Hz) is estimated in the PT data at x=42 m (Fig. 9b. This could be explained by two factors and it is not certain which prevails: an underestimation in the model of the transfer of energy to sub-harmonics between x=0 and 42 m or a more efficient absorption of outgoing waves at the numerical paddle than in the real flume. The energy peaks and the spectrum tail along the wave flume are well represented everywhere else, indicating that the model is able to simulate the breaking process and the transfer of energy to higher/lower frequencies. Similar performance has been observed by Morgan et al. [59] in their modelling of wave transformation over submerged bar with up to 8th order harmonics correctly simulated.

The observed agreement between the RT and the Guza84 approach are somewhat surprising for two main reasons: 1) the previously observed differences at the wave-by-wave scale between the pressure-derived surface elevation and the model output close to break point (around 30% of H, Fig. 2) is not evident in the spectral domain, and 2) while the Guza84 method, is thought to be inappropriate for use in highly non-linear surf zone waves, the current results indicate that it can be applied in the surf zone with reasonable results.

4.2. Intrawave variability of wave heights and wave height to water depth ratio

Fig. 10a and b present the cross-shore evolution of the modelled individual wave height H for the total and incoming signals, from the A6-mono and A7-mono tests. Similar to that observed in the $\eta(x, t)$ diagram presented in Fig. 8a, the reflected components of the waves are clearly observable in the cross-shore evolution of H. In the total signal

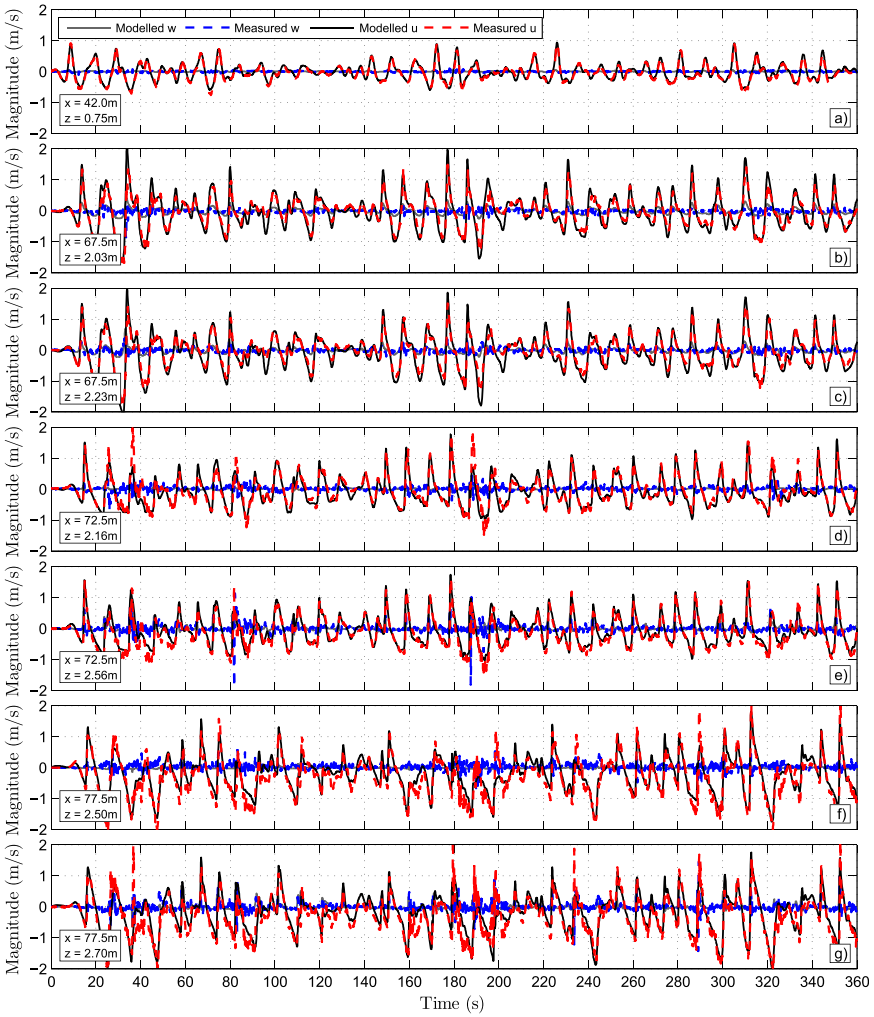

Fig. 6. Validation of the modelled hydrodynamics at the EMCM locations for the A6-01 wave test, for the first 320 s of the simulation. Modelled horizontal U and vertical V timeseries are shown against measurements at one location in the shoaling region and six in the surf zone.

$\eta(x, t)$ diagram (Fig. 8a), the first modelled wave after reflection influences the second, third and fourth incident waves at cross-shore positions of approximately x=71 m, 44 m and 14 m. The surface elevation at these locations is temporarily increased due to the presence of a reflected wave crest, and this leads to an apparent net increase in H from total signal at these cross-shore locations, while the values from the incoming signals obtained from the RT present gradually increasing H values in the shoaling region, as it should be expected. Similarly, the passage of troughs also influence H values by decreasing the surface elevation temporarily.

The observed effect of reflected waves on individual wave height is also present in γ values which are expressed as $\gamma = H/\overline{h}$ (Fig. 10c and d). Since the first modelled wave is propagating in a calm wave flume, its properties are not altered by any reflected component: γ_{tot} and γ_{inc} should therefore be similar. This is observed in Fig. 10a and b where the incoming and total values match at all positions (gray lines and dots), and in the scatter plots of Fig. 10c and d, where gray dots are close to the 1:1 agreement. While for the subsequent waves in the test there are differences between γ_{tot} and γ_{inc} values of up to 35% in the shoaling area, this reduces to around 25% closer to the break point, which is defined as the location of the maximum wave height for each propagating wave (x=71 m, for both monochromatic tests).

A similar wave-by-wave approach was performed for the A6-01 irregular test case and the results can be observed in Fig. 11. Fig. 11a shows the cross-shore evolution of $\gamma_{s,tot}$ and $\gamma_{s,inc}$, based on significant wave height H_s and mean water depth. In the shoaling area, the two ratios present identical evolution, demonstrating little influence of reflection on averaged breaker indexes in that zone. Just offshore of the bar, the values computed from the incoming signals are slightly larger than those from the total signal, while over the bar the opposite occurs. The most significant difference is visible on the terrace (x = 75 − 78 m), where incoming values are approximately 15% greater.

Individual γ and $\gamma_{tr} = H/h_{tr}$, where h_{tr} is the water depth below the wave trough, are shown in Fig. 11b-e for incoming and total signals. Overall, the values computed from the incoming signal are less variable; this can be seen from the slightly smaller error bars and more 'organized' lines, showing lower intrawave variability. The scatter plots of Figs. 11f and g allow a comparison of the different definitions of γ and suggest that variations up to 20% and 40% are common for γ and γ_{tr} respectively which is comparable to that found for the monochromatic cases (Fig. 10c and d).

The alternate effect of reflected wave crests and troughs on the incident waves for the irregular wave test is similar to that observed for the monochromatic wave tests. This behaviour supports the concept of quasi-standing waves previously observed by Hoque et al. [17] for shorter waves. The interactions of two progressive waves travelling in opposite direction, with the same period but different amplitude (due to wave breaking and friction), generates quasi-antinodes and quasi-nodes at the location where the incident and reflected waves are in phase and out of phase respectively. This concept has been investigated for the A6-01 irregular wave test. Fig. 12 shows the cross-shore evolution of the ratio of total and incoming variance density spectra

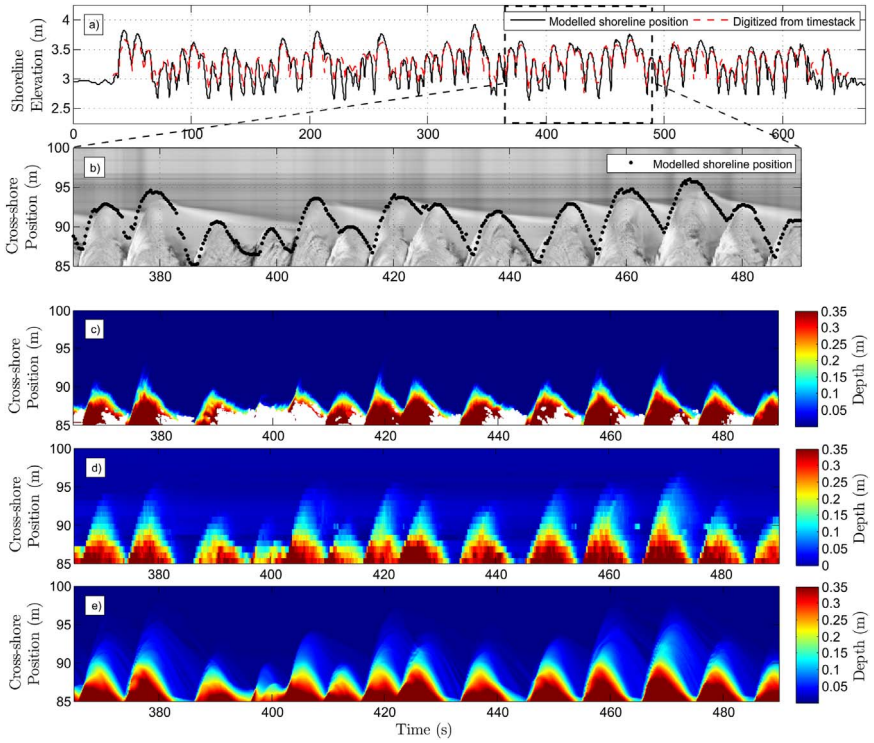

Fig. 7. Validation of the model in the swash zone: a) Modelled shoreline elevation and digitised shoreline elevation from the ARGUS video camera timestack are shown for the entire wave test, b) ARGUS Video camera timestack along with the modelled shoreline cross-shore position for a 2 min window, c) Water depths measured by the swash zone TLS, d) Water depths measured by the array of ultrasonic BLS and e) Modelled water depths. (For interpretation of the references to color in this figure legend, the reader is referred to the web version of this article.)

$S_\eta/S_{\eta_{inc}}$ for sea/swell frequencies. This ratio indicates the presence of reflected wave energy: a ratio greater than 1 corresponds to the presence of a reflected wave crest, while a ratio lower than 1 corresponds to the presence of a reflected wave trough. For relatively low frequencies ($f \leq 0.2$ Hz), a node/antinode pattern is observed along the wave flume. In particular, for the frequency of the monochromatic wave tests (f=0.083 Hz), a very similar node/antinode system as observed in Fig. 10 is found during the irregular wave run: antinodes due to superposed crests are found at around x=75 m, x=53 m and x=24 m, and discrepancies are mainly explained by the different foreshore slope (Table 1). It was suggested for the monochromatic wave tests that partially standing waves were responsible for the intrawave variability of H and hence γ (Fig. 10). The results presented in Fig. 12 suggest that similar behaviour is observed for irregular waves, and for relatively high frequencies.

4.3. Generation of swash-based reflections

The reflected waves studied here in the sea/swell frequency are thought to be 'generated' primarily by the seaward propagating mass fluxes present in the strong swash backwashes. The term swash-based is therefore used to describe this type of reflection. This concept has been investigated by relating the energy of the tracked reflected waves to the maximum potential energy present in the swash preceding the 'generation' of that reflected wave. The two energy concepts are expressed as follows:

$$E_{ref} = \rho g \int_0^L \eta_{ref}^2(x)dx \tag{5}$$

$$\max_t E_{p,swash}(t) = \rho g \int_0^{R(t)} h(x,t)z(x,t)dx \tag{6}$$

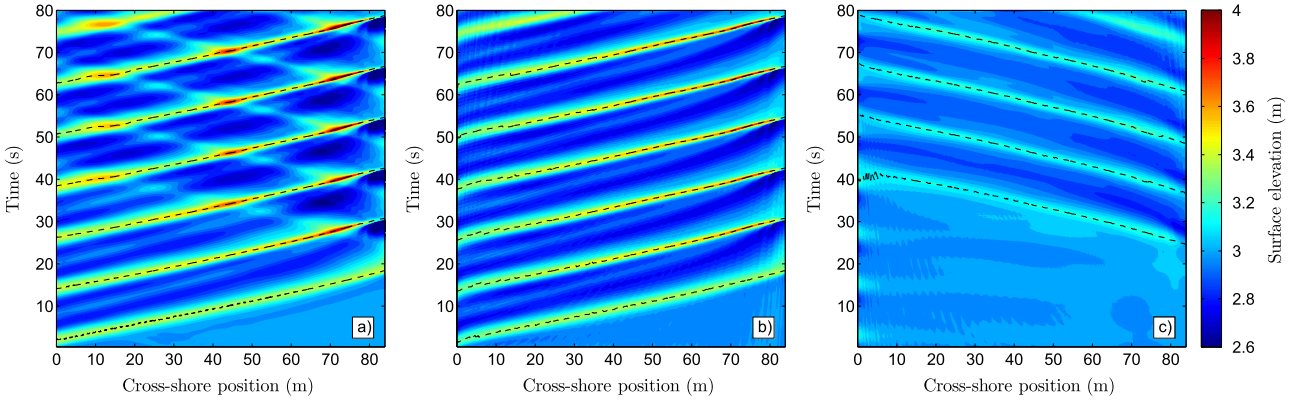

Fig. 8. Incoming/outgoing signal separation of the modelled surface elevation using the RT: a) $\eta(x,t)$ diagram of the modelled surface elevation for the A7-mono wave test; b) $\eta_{inc}(x,t)$ diagram of the incoming signal; c) $\eta_{ref}(x,t)$ diagram of the outgoing signal. In every panel, the dashed black lines show the individual waves path, tracked with the methodology presented in Section 4.2.

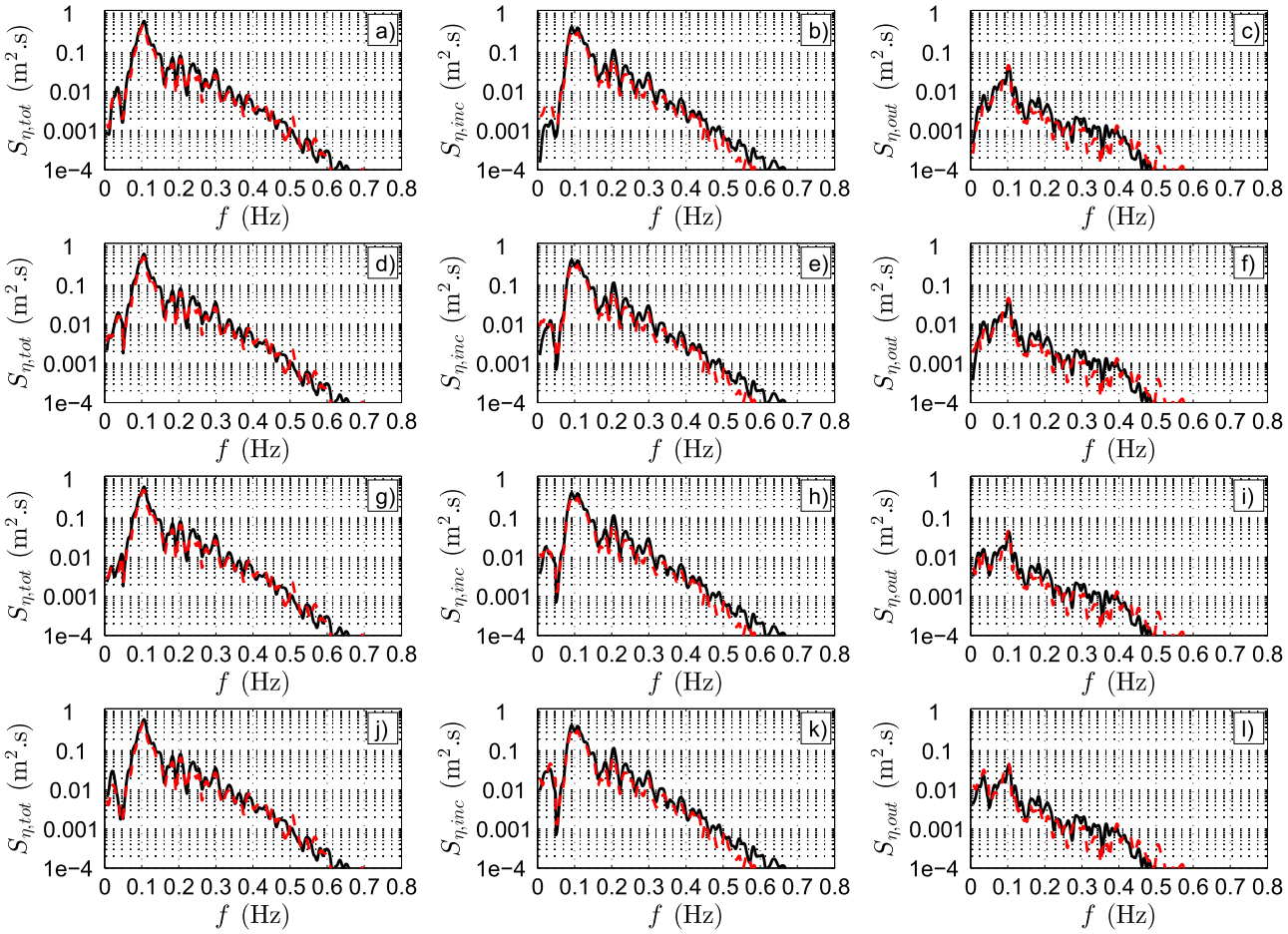

Fig. 9. Comparison of the modelled surface elevation spectra (black line) along the wave flume against measurements from pressure-derived data (red dashed line), for total (left column), incoming (central column) and outgoing (right column). The modelled total signal was separated using the RT, while the measured total signal was separated with the Guza84 method. Comparisons are performed at the following cross-shore locations: a-b-c) x = 42 m, d-e-f) x = 67.5 m), g-h-i) x = 72.5 m) and j-k-l) x = 77.5 m).

where L is the wavelength, $R(t)$ is the time-varying shoreline position, $h(x, t)$ the water depth and $z(x, t)$ the height above the reference for null potential energy taken as MSL. In the potential energy formulation from Eq. (6), $z(x, t)$ is the mid flow depth: $z(x, t) = z_{bed}(x) + h(x, t)/2$, where $z_{bed}(x)$ is the bed elevation at the cross-shore position x. A sketch describing the terminology used in Eqs. (5) and (6) is presented in Fig. 13.

Fig. 14 shows the comparison of the two energy expressions for a range of both validated and unvalidated test cases. Although not validated in this paper, the A1-mono, A2-mono and A4-mono wave tests from the BARDEXII experiments were run for this investigation in order to have a wider range of beach and wave characteristics (see Table 1). Additionally, two further monochromatic cases using the same H_s and beach conditions as A7-mono, but with different wave periods were modelled (see Table 1). For every regular case, the ensemble-averaged energy from the tracked reflected wave (Eq. (5), estimated between x=15 m and $x = 15 + L$ m) is compared to the ensemble-averaged potential energy contained in the preceding swash event ((Eq. (6)). For the irregular run, a subset of 5 individual waves was extracted. For the beach slopes and wave conditions examined here, a clear correlation between the two energy formulations is observed in Fig. 14 with the potential energy in a swash event consistently double that of the reflected wave that this event generates.

This result suggests that it is possible to estimate the energy and height of individual reflected waves based on the monitoring of foreshore bed levels and the time-varying surface elevations (leading to water depths and swash excursion, the two required parameters). Field deployments of TLS in the swash zone such as in Martins et al. [21,60] could use this relationship to estimate the bulk of energy reflected from the beach. Further investigation is required to completely validate this hypothesis, and to explain the presence of the 0.5 coefficient of proportionality observed in Fig. 14, though this is thought to be closely linked to the beach gradient and hence the mass flux in the backwash.

4.4. Cross-shore evolution of reflection coefficients

To the authors' knowledge, Baquerizo et al. [9] were the first to study the cross-shore variation of the reflection coefficient in the sea/swell range of frequencies, defined as the ratio of incoming and outgoing wave energy. Using various methods to separate incoming and outgoing signals, they measured increasing reflection coefficient values through the surf zone and suggested that to minimize the uncertainty introduced by this variation, representative values should be estimated seaward of the break point. A numerical model based on an energy balance, taking into account the incident wave dissipation and reflection from slope was developed by Baquerizo et al. [61] to predict local reflection coefficients. Although it showed very good agreement seaward of the break point it overestimated the reflection coefficient in the surf zone. Discrepancies in the surf zone are thought to be due to the expression of the reflected wave energy fluxes, directly linked to the incoming fluxes and the rate of dissipation. To illustrate this, the energy fluxes defined using linear theory as $F = H^2c$, where c is the wave celerity [61], for the incident and reflected waves from the A6-mono and A7-mono tests are shown in Fig. 15a. While the energy fluxes of reflected waves are approximately constant, meaning that

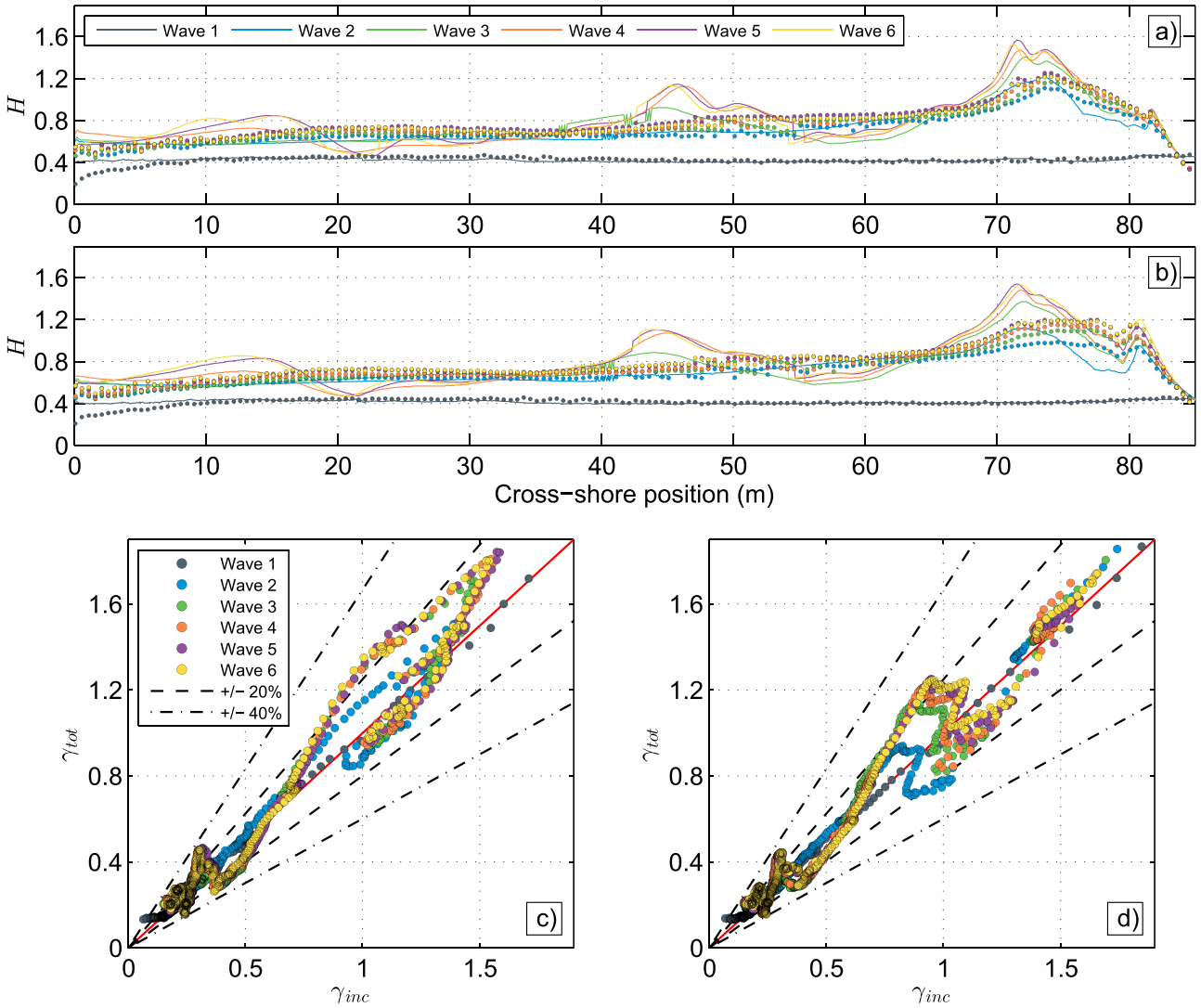

Fig. 10. Results from the wave-by-wave analysis on modelled total and incoming signals ($\eta(x, t)$ and $\eta_{inc}(x, t)$) from the A6-mono and A7-mono wave tests. Panels a) and b) represent the wave height evolution extracted from the total (continuous lines) and incoming (dots) signals for the A6-mono and A7-mono wave tests respectively. Panels c) and d) represent the corresponding γ scatter plots for the A6-mono and A7-mono wave tests respectively (values from the total signal against values from incoming signal). In the four panels, the 6 modelled waves are shown, and the same colours are used in the line/dots for the wave numbering; ± 20% and ± 40% lines are also represented in the scatter plots as dashed and dot-dashed lines respectively.

waves are deshoaling as c increases with increasing depths, the incident waves show a net increase in energy flux landward of $x = 40 - 50$ m. This occurs when wave celerity cannot be described anymore by linear wave theory and corresponds to where wave non-linearities become important (high Ursell number). This overestimation in the incident wave energy fluxes when non-linearities become significant leads, for a given dissipation rate, to an overestimation of the reflected wave energy as defined by Baquerizo et al. [61]. This is consistent with the larger reflected fluxes found in the surf zone by Baquerizo et al. [9] (see their Fig. 8).

The direct ratio between incident and reflected individual wave heights is shown in Fig. 15b, for both monochromatic tests. It is shown that up to the break point (x=71 m), the ratio remains reasonably constant with a slight decreasing trend for both tests. This is explained by the shoaling incident waves dominating over the deshoaling reflected waves, observed in Fig. 15a. Landward of the break point $x = 71 - 75$ m, and as previously found by Baquerizo et al. [61], the ratio rapidly increases due to the sudden decrease in the wave height after breaking. It is hard to infer from the present dataset what would happen with a wider surf zone and at distances further from the break point. It is natural though to hypothesise an increase of H_{ref}/H_{inc} towards a value which is a function of the wave steepness and the foreshore slope. The energy dissipation rate and the width of the surf zone after break point indeed limit the maximum H_{inc} that can be reflected from a beach, for a given foreshore slope and incident wavelength [56].

5. Discussion

5.1. Break point

The differences observed in the γ values under the presence of reflected waves can be of great significance for numerical models or the parameterisation of wave energy across the surf zone. For instance, a shift seaward or landward of the break point due to the presence of reflected waves will change the energy dissipation patterns across the surf zone, and can affect the position of bar for models supported by the break point hypothesis for sandbar generation [62].

For both monochromatic wave tests, H computed from the total signal reaches its maximum at the same location ($x = 71$ m), see Fig. 10a and b. However, if only the incoming signal is considered, the maximum wave height is reached around x=74 m for both tests,

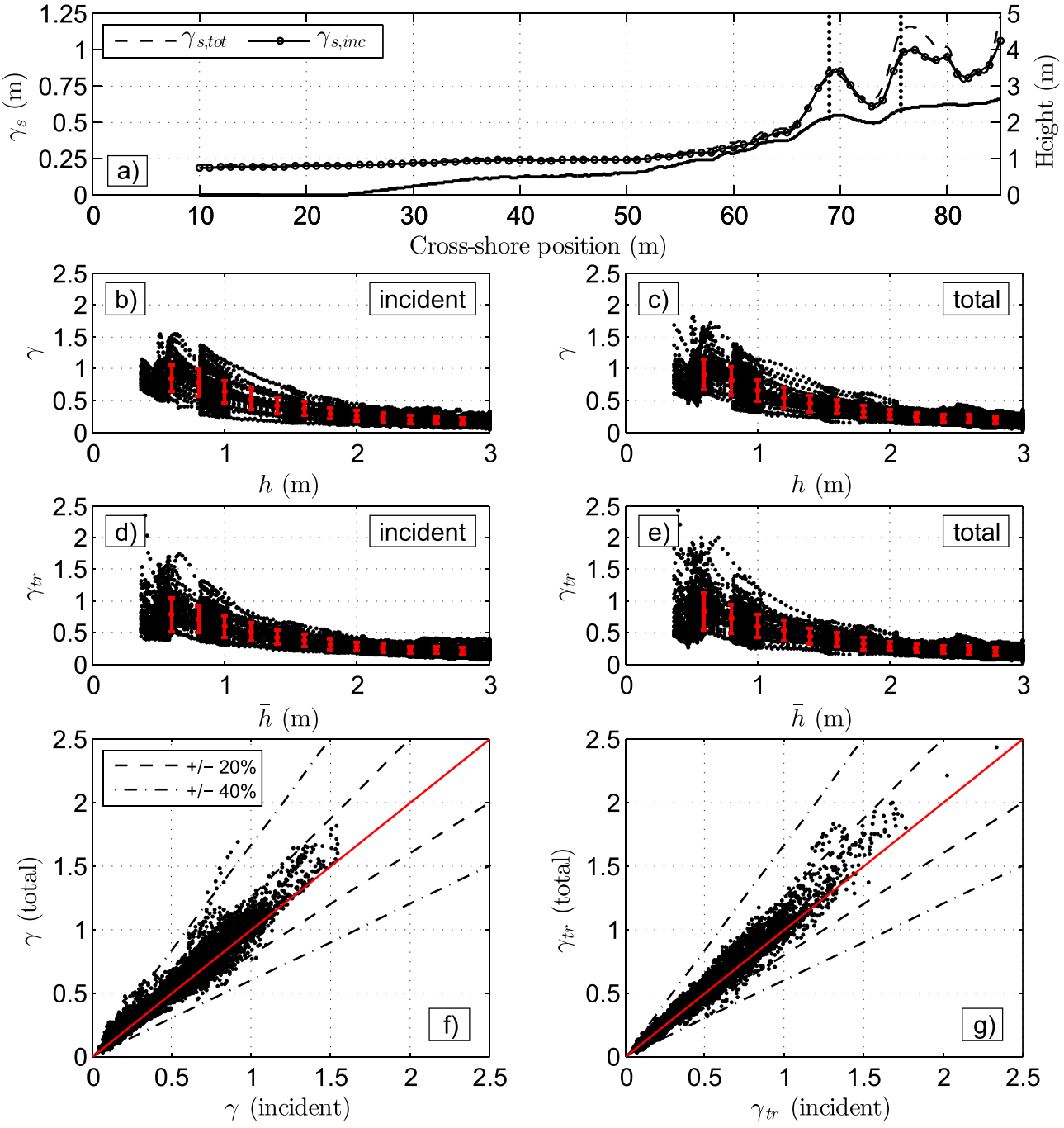

Fig. 11. Results from the wave-by-wave analysis on the total and incoming signals ($\eta(x, t)$ and $\eta_{inc}(x, t)$) from the A6-01 irregular wave test. Panel a) shows the cross-shore evolution of the significant wave height to depth ratio γ_s computed from the total (dashed line) and incoming (circled line) signals respectively. The two break points defined as the maximum significant wave height are also shown as vertical dotted lines. Panels b) and c) show the individual γ values computed from the total and incoming signal. Panels d) and e) show the individual γ_{tr} values computed from the total and incoming signal using the water depth below trough h_{tr}. For these 4 scatter plots, standard deviation of the mean are shown as error bars, using bins of 0.2 m. Panels f) and g) represent the corresponding γ and γ_{tr} scatter plots. In these, ± 20% and ± 40% lines are also represented as dashed and dot-dashed lines respectively.

though it is noted that no strong peak is observed for A7-mono and the wave height remains constant over the low-sloping terrace. If the break point is defined as the location of maximum wave height as used in this study, the results suggest that the incident wave break point occurs further landward. Although no evidence of a direct influence from the reflected wave field on the wave energy dissipation or the breaking onset of incident waves is shown, the detection of the break point with the present definition is affected and therefore biased by the presence of reflected waves.

For the irregular wave test, the presence of reflected waves does not seem to influence the location of the break point as it is observed that the peak values of total and incoming significant wave height computed over sea/swell range of frequencies H_s occur at the same location: $x = 68.5$ m and $x = 75.4$ m (Fig. 11a). At the inner breakpoint, there is a discrepancy of up to 15% between the gamma values derived from the total and incoming signals and therefore the presence of reflected wave may explain previously observed discrepancies between existing breaker index datasets [63]. Further effort is therefore required to account for the influence of wave reflection on gamma in order to obtain a better description of cross-shore evolution of incident wave height

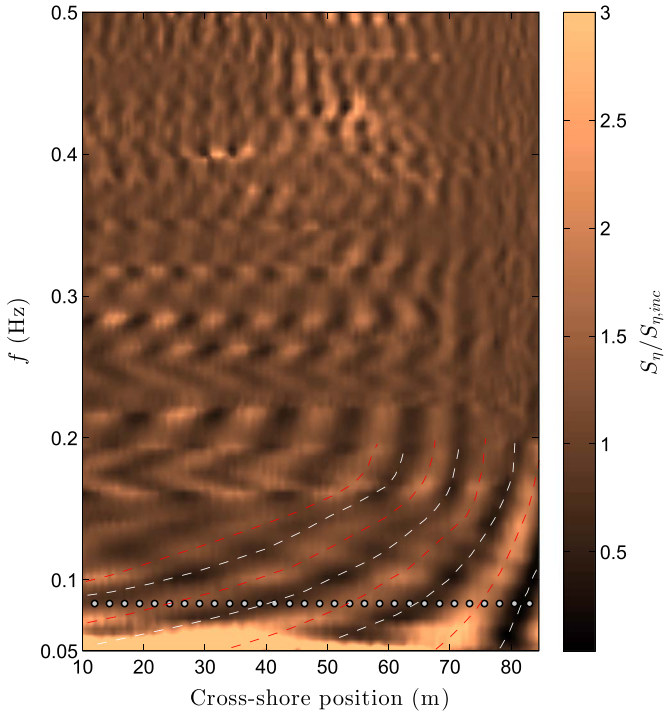

Fig. 12. Cross-shore evolution of the ratio of variance density spectra computed on total and incoming surface elevation signals. For $f \leq 0.2$ Hz and for each frequency, the locations of two types of antinodes are shown as white (incident and reflected wave troughs superposed) and red (incident and reflected wave crests superposed) dashed lines. The frequency corresponding to the A6-mono and A7-mono wave tests is also shown by the grey dots. (For interpretation of the references to color in this figure legend, the reader is referred to the web version of this article.)

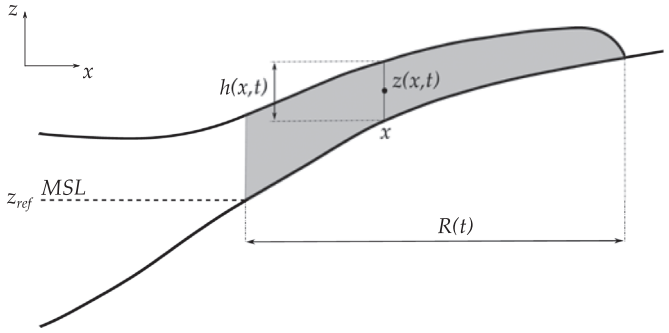

Fig. 13. Sketch of a typical swash event, at a time t. Mean Sea Level (MSL) defines the elevation reference z_{ref} for the potential energy definition in Eq. (6). The intersection between MSL and the bed also defines the origin to estimate the time-varying horizontal shoreline position $R(t)$. x defines the cross-shore location, $h(x, t)$ the water depth at x and time t, $z(x, t)$ the middle point of the water column at x.

under reflective conditions.

5.2. Influence of wave reflection on time-averaged surf zone parameters

The results presented in Fig. 12 suggest that wave reflection in the sea/swell range of frequencies in a reflective environment can influence the surf hydrodynamics at the wave-by-wave scale through the formation of multiple quasi-node/antinode system, affecting orbital velocities. Further influence at longer timescales is discussed here, in terms of undertow, wave setup and horizontal velocity skewness.

5.2.1. Undertow

Horizontal current velocities from the A6-01 test were separated using linear theory (see Section 4.1), and time-averaged to obtain the

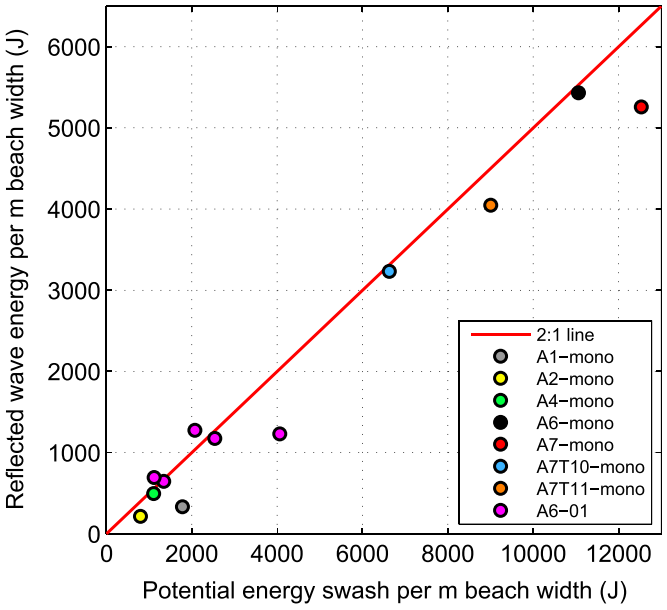

Fig. 14. Comparison between reflected wave energy (Eq. (5)) and maximum potential energy in the preceding swash event (Eq. (6)) for a range of validated and unvalidated test cases detailed in Table 1.

contribution of both incoming and outgoing wave-induced hydrodynamics on the undertow. Fig. 16 shows the result of this separation by illustrating the contribution of the outgoing wave field on the undertow along the wave flume. At the four locations where current velocities measurements are available (x=42, 67.5, 72.5 and 77.5 m), modelled mean horizontal flow magnitude is shown against measurements (Fig. 16a-d). The ratio $|\overline{U_{out}}|/|\overline{U_{inc}}|$ shown as a contour plot in Fig. 16e represents the relative contribution of the outgoing wave field on the mean return flow. Although, over-predicted in the mid-column at x=67.5 m and slightly underestimated at x=77.5 m, the modelled undertow shows good agreement with data, in terms of magnitude and vertical structure.

Consistent with previous work [64], the vertical structure of the undertow evolves with the water depth across the shoaling area and the surf zone. Where non-linearities are small ($\gamma_s \sim O(0.2)$ and low Ursell number), the undertow is weak, and rather vertical-uniform close to the bed. In this region, the undertow is dominated by the outgoing wave field (Fig. 16e), which triggers an offshore-directed mean horizontal current. With reducing depth and hence increasing non-linearities (between x=35 m and 50 m) the waves are shoaling and the undertow remains weak and seaward directed. In this region the incoming and outgoing wave field contribute roughly equally to the mean flows ($|\overline{U_{out}}|/|\overline{U_{inc}}| \approx 1$ in Fig. 16e). As waves propagate closer to the bar crest, the beach becomes much steeper, and the undertow magnitude becomes much stronger, with its maximum reached at mid-depth.

The ratio shown in Fig. 16e exhibits a narrow band in the lower 10 cm of the water column and seaward of the bar (focussing on the region between x=66 m and 69 m immediately adjacent to the bed where $|\overline{U_{out}}|/|\overline{U_{inc}}| \approx 0.4$) where reflection seems to have an important influence on the undertow. In this narrow band, the mean flow induced by outgoing waves is onshore-directed close to the bed (Fig. 16b), and has the effect of almost balancing the offshore-directed mean flow induced by the incoming wave field, leading to almost zero mean flow adjacent to the bed. This is thought to have an influence on bar morphology and will be further discussed in Section 6. Except in this narrow band, the incoming wave field is mostly responsible for the mean return flow around the bar location, indicated by the region where $|\overline{U_{out}}|/|\overline{U_{inc}}|$ is close to zero between x=62 and 72 m.

The strengthening of the undertow by the outgoing wave field, can

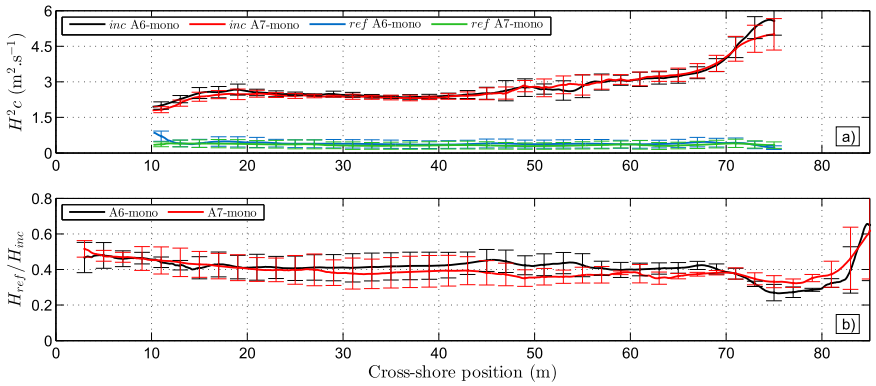

Fig. 15. Cross-shore evolution of reflection coefficient based on individual wave properties: a) individual wave incident and reflected energy fluxes and b) individual incident and reflected wave height ratio for the A6-mono and A7-mono tests. The value for each run represents the ensemble-average of the four first waves, since only four reflected waves could be tracked (as seen in Fig. 2c). Standard deviation of the ensemble-average values are shown every two meters in the cross-shore direction, as error bars. For the fluxes expression, wave celerity was estimated for each wave on an individual basis, using the tracking method described in Section 3.2.

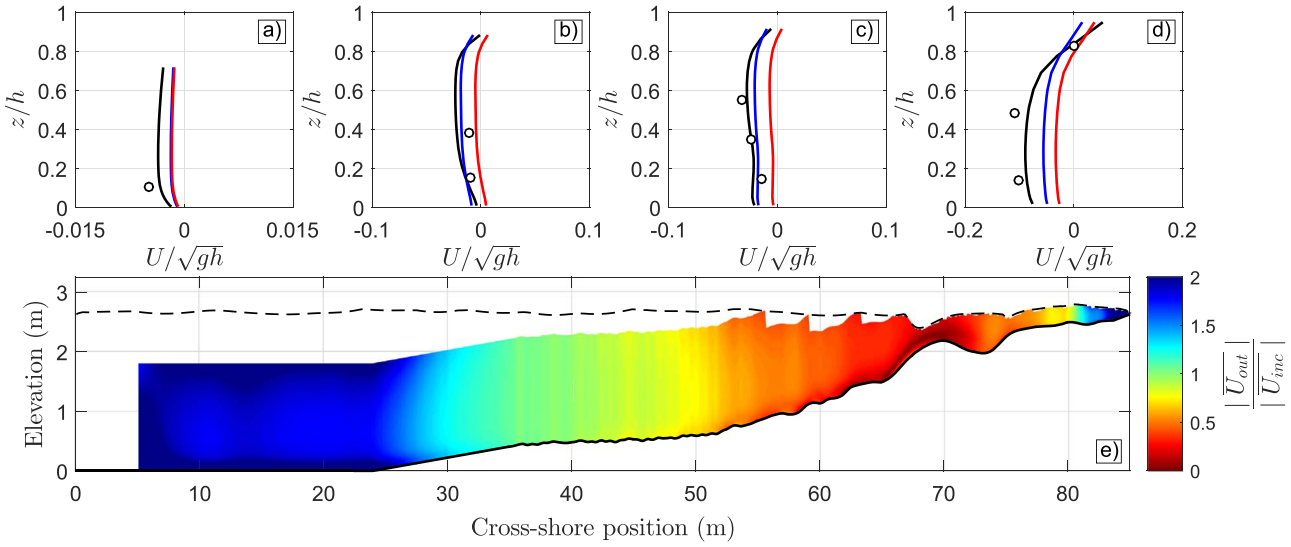

Fig. 16. Vertical structure of the modelled undertow along the flume for the A6-01 wave test. The top panels show the modelled undertow from total (black line), incoming (blue line) and outgoing (red line) signals at: a) x = 42 m, b) x = 67.5 m, c) x = 72.5 m and d) x = 77.5 m. Experimental data from the EMCM are shown as circles. Panel e) shows a contour plot of the outgoing signal contribution on the undertow structure, compared to the incoming contribution. The black dashed line corresponds to the minimum surface elevation reached, and any data from above that limit has been removed to not bias the time-average. (For interpretation of the references to color in this figure legend, the reader is referred to the web version of this article.)

partially be explained by the offshore-oriented Stokes drift that it generates and a change in the wave setup [65]. Indeed, Fig. 17a) suggests that the presence of reflected waves significantly reduces the setdown generated by the breaking of incident waves in the region $x = 72 - 80$ m. Landward and seaward of this region, the setup induced by the outgoing field predominates over that from the incoming field, which is consistent with the observations made on the undertow (Fig. 16d). The undertow is known to influence cross-shore sediment transport, as it plays an important role in the offshore/onshore bar migration [66,67] and/or in the resuspension of sediment in the water column [68]. Fig. 16 for instance suggests that the presence of the outgoing wave field helps to stabilise the bar by weakening the offshore directed mean flow at the bottom of the water column. Although it is consistently offshore-directed, the present results show that the nature of the undertow - at least in reflective environments - is more complex that it was thought before, e.g. in terms of temporal structure with a contribution from incident and reflected waves acting with different phasing.

5.2.2. Skewness

Flow skewness and wave asymmetry have been shown by many researchers to contribute to onshore-directed sediment fluxes, therefore balancing the effect that undertow has on surf zone morphodynamics, see for instance Elfrink et al. [15], Elgar et al. [69], Silva et al. [70]. Fig. 17b shows the surface elevation asymmetry - defined as $A_s = -\overline{\mathcal{I}m(\mathcal{H}(\eta))^3}/\overline{\eta^2}^{3/2}$ where $\mathcal{I}m$ is the imaginary part of the Hilbert transform $\mathcal{H}$ of the surface elevation - and Fig. 17c-e show the flow velocity skewness along the wave flume, computed from the total, incoming and outgoing wave-induced velocity fields. Two striking observations emerge from this analysis: 1) near-zero skewness from the incoming component on top of the bar and on the terrace (Fig. 17c), and 2) the negative skewness of the outgoing field (Fig. 17d) that therefore generates a negative total skewness over the terrace ($x = 75 - 82$ m, see Fig. 17b). The positive skewness seaward of the bar trough and negative skewness landward, along with strong surface elevation asymmetry observed in Fig. 17a are thought to explain the 'filling' of the trough observed after the A6-01 test under similar wave conditions [34]. This is consistent with the findings of Grasso et al. [71].

Although, no obvious influence of the multiple quasi-node/antinode system can be observed in the different skewness fields, it is thought to be of importance. Bowen [72] suggested that nodes/antinodes of standing infragravity waves and their associated drift velocities could trigger the generation/migration of bar towards an equilibrium profile.

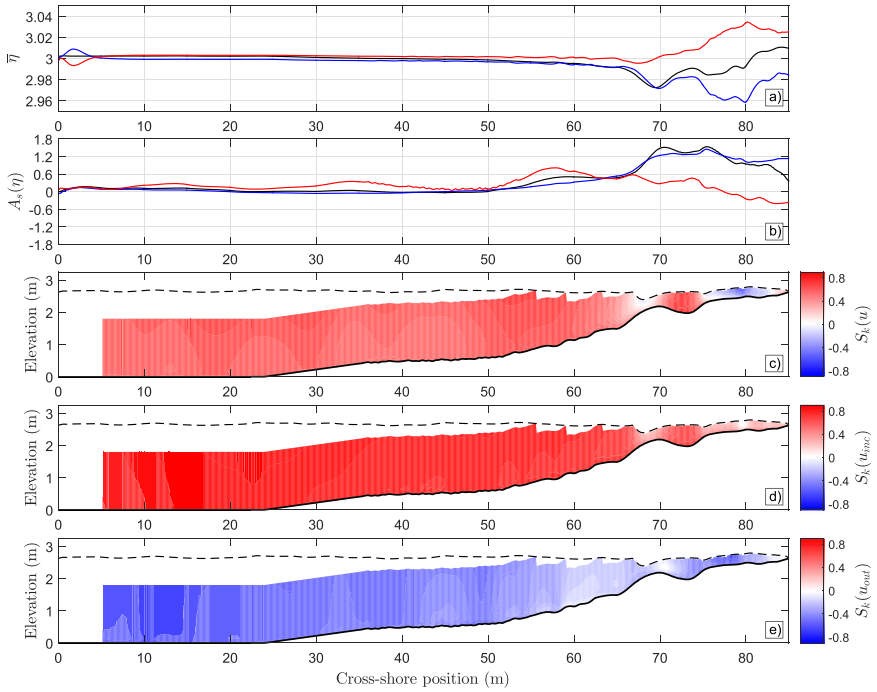

Fig. 17. Evolution of modelled time-averaged surf zone parameters along the wave flume. Panel a) shows the modelled time-averaged surface elevation (wave setup) for the total, incoming and outgoing signal (black, blue and red lines respectively). Panel b) shows the surface elevation asymmetry for the total, incoming and outgoing signal (black, blue and red lines respectively). Panels c), d) and e) show contour plots of the skewness computed from the total, incoming and outgoing horizontal velocity fields, respectively. The black dashed line in panels c-e) corresponds to the minimum surface elevation reached, and any data from above that limit has been removed to not bias the skewness computation. (For interpretation of the references to color in this figure legend, the reader is referred to the web version of this article.)

This was confirmed numerically by Bernabeu et al. [73] who obtained improved model skill in predicting beach equilibrium profiles by accounting for wave reflection. Further verification was obtained in field conditions for sea/swell frequencies by Sánchez-Badorrey et al. [74] who observed the generation of a multiple bar-trough system in front of a newly installed seawall which matched the quasi-node/antinode positions of the peak frequency. Similarly, Alsina et al. [75] observed a reduced offshore bar migration rate when conditions in the swash were more dissipative: if reflection occurs earlier, the antinode location slightly shifts offshore compared to the location for a more dissipative swash, generating a different sediment convergent point. Alternatively, this can also be explained by the more intense backwashes observed that potentially suspend more sediment in the inner surf. Combined with the stronger undertow under more reflective conditions (Fig. 16), it can possibly promote higher offshore-directed sediment transport rates. As noted by Grasso et al. [71], despite recent effort in that regard, it is difficult to isolate individual physical processes that might affect sediment transport rates in the surf zone. Although rarely considered as such, wave reflection in the sea/swell range of frequencies in reflective environments is clearly playing a role in the surf zone hydrodynamics at various time scale, which in turn affect the morphodynamics.

6. Conclusions

In this paper, a RANS numerical model based on the IHFOAM library [43] has been validated and used to study the influence of swash-based wave reflection in the sea/swell range of frequencies on surf zone hydrodynamics at the wave-by-wave and wave tests temporal scales. A TLS dataset of breaking waves has been used for the first time to validate the modelled wave shape at various stage of breaking. This highlighted the important wave-by-wave discrepancies (wave height and skewness) when using linear theory to retrieve the surface elevation from the measured pressure signal, close to the break point.

The RT was successfully applied to the modelled free surface elevation to separate incoming and outgoing signals. A wave tracking algorithm was used to isolate individual waves and demonstrated that reflected waves induce intrawave variability of individual incident wave properties such as the wave height, and the wave height to water depth ratio, through the generation of quasi-standing waves. Variations of up to 35% and 15% are observed for individual and spectral values of wave height to water depth ratios respectively. This renders the extraction and the study of incident wave properties more difficult, and must be considered when parameterising wave reflection in numerical models of nearshore circulation. By tracking individual reflected waves, a direct link between the potential energy of swash flows and the reflected wave energy has been demonstrated. This has two main implications: 1) the potential to use measurements of swash depths to estimate the energy of individual reflected waves, and 2) a good representation of swash mass fluxes is required to accurately model surf zone hydrodynamics [76].

Using the Guza84 approach, the incoming and outgoing components of the modelled horizontal flow velocities were computed along the wave flume in order to study the contribution of each component to the mean return flow (undertow) and higher velocity moments (skewness). It was demonstrated that the presence of strong reflective conditions were promoting the undertow, by strengthening its magnitude almost everywhere in the wave flume except offshore of the bar crest, where the outgoing components induce an onshore-directed streaming close to the bed. This phenomenon, added to the convergence points created by the observed quasi-standing waves and the influence of reflection on velocity skewness is thought to influence sediment transport rates and their variation along the beach profile, contributing to bar generation/migration.

Acknowledgements

This work was supported by the University of Bath, through a URS scholarship, and by the EPSRC-funded project EP/N019237/1 “Waves in Shallow Water: A new approach based on high-frequency remote

sensing and wave-by-wave analysis". The two anonymous reviewers are greatly acknowledged for their constructive comments on the paper. The BARDEXII data set used in this study is available from http://www.hydralab.info, and it was obtained with the support by the European Community's 7th Framework Programme through the grant to the budget of the Integrating Activity HYDRALAB IV, contract no. 261520.

References

[1] J.R. Miles, P.E. Russell, D.A. Huntley, Field measurements of sediment dynamics in front of a seawall, J. Coast. Res. 17 (2001) 195–206.
[2] M. Brocchini, T.E. Baldock, Recent advances in modeling swash zone dynamics: influence of surf-swash interaction on nearshore hydrodynamics and morphodynamics, Rev. Geophys. 46 (2008). http://dx.doi.org/10.1029/2006RG000215.
[3] B. Zanuttigh, J.W. van der Meer, Wave reflection from coastal structures in design conditions, Coast. Eng. 55 (2008) 771–779. http://dx.doi.org/10.1016/j.coastaleng.2008.02.009.
[4] C.R. Iribarren, C. Nogales, Protection des ports, XVIIth International Navigation Congres, 1, 1949.
[5] A. Miche, Le pouvoir réfléchissant des ouvrages maritimes exposés à l'action de la houle, Ann. Des. Ponts Et. Chauss-. 121 (1951) 285–319.
[6] J.A. Battjes, Surf similarity, in: Proceedings of the 14th Conference on Coastal Engineering, Copenhagen, Denmark, 1974, pp. 466–480.
[7] S.A. Hughes, J.E. Fowler, Estimating wave-induced kinematics at sloping structures, J. Waterw. Port. Coast. Ocean Eng. 121 (1995) 209–215.
[8] J.R. Miles, P.E. Russell, Dynamics of a reflective beach with a low tide terrace, Cont. Shelf Res. 24 (2004) 1219–1247. http://dx.doi.org/10.1016/j.csr.2004.03.004.
[9] A. Baquerizo, M.A. Losada, J.M. Smith, N. Kobayashi, Cross-shore variation of wave reflection from beaches, J. Waterw. Port. Coast. Ocean Eng. 123 (1997) 274–279.
[10] S. Elgar, R.T. Guza, Observations of bispectra of shoaling surface gravity waves, J. Fluid Mech. 161 (1985) 425–448. http://dx.doi.org/10.1017/S0022112085003007.
[11] A.T.M. de Bakker, T.H.C. Herbers, P.B. Smit, M.F.S. Tissier, B.G. Ruessink, Nonlinear infragravity wave interactions on a gently sloping laboratory beach, J. Phys. Oceanogr. 45 (2015) 589–605. http://dx.doi.org/10.1175/JPO-D-14-0186.1.
[12] A. Sheremet, R.T. Guza, S. Elgar, T.H.C. Herbers, Observations of nearshore infragravity waves: seaward and shoreward propagating components, J. Geophys. Res.: Ocean. 107 (2002). http://dx.doi.org/10.1029/2001JC000970 (10–1–10–10).
[13] S. Elgar, T.H.C. Herbers, R.T. Guza, Reflection of ocean surface gravity waves from a natural beach, J. Phys. Oceanogr. 24 (1994) 1503–1511 (10.1175/1520-0485(1994)(024 < 1503:ROOSGW > 2.0.CO;2).
[14] R. Almar, P. Catalan, R. Ibaceta, C.E. Blenkinsopp, R. Cienfuegos, M. Villagran, J.C. Aguilera, B. Castelle, Swash zone based reflection during energetic wave conditions at a dissipative beach: Toward a wave-by-wave approach, in: Proceedings of the 34th Conference on Coastal Engineering, Seoul, Korea, 2014.
[15] B. Elfrink, K.A. Rakha, R. Deigaard, I. Brøker, Effect of near-bed velocity skewness on cross shore sediment transport, in: Proceedings of the 4th International Symposium on Coasting Engineering and Science of Coastal Sediment Processes (ASCE), Hauppauge, New York, United States, 1999, pp. 33–47.
[16] J.C. Doering, B. Elfrink, D.M. Hanes, B.G. Ruessink, Parameterization of velocity skewness under waves and its effect on cross-shore sediment transport, in: Proceedings of the 27th Conference on Coastal Engineering, Sydney, Australia, 2000, pp. 1383–1397.
[17] M.A. Hoque, T. Asano, M.A.L. Neshaei, Effect of reflective structures on undertow distribution, in: Proceedings of the Fourth International Symposium on Ocean Wave Measurement and Analysis, Waves 2001, San Francisco, California, United States, 2002, pp. 1042–1051. http://dx.doi.org/10.1061/40604(273)106.
[18] J.A. Battjes, J.P.F.M. Janssen, Energy loss and set-up due to breaking of random waves, in: Proceedings of the 16th Conference on Coastal Engineering, Hamburg, Germany, 1978, pp. 569–587.
[19] B. Raubenheimer, R.T. Guza, S. Elgar, Wave transformation across the inner surf zone, J. Geophys. Res.: Ocean. 101 (1996) 25589–25597.
[20] N. Sénéchal, Etude de la propagation des vagues au-dessus d'une bathymétrie complexe en zone de surf, (Ph.D. thesis), École doctorale sciences du Vivant, géosciences, sciences de l'environnement, Université de Bordeaux I, 2003.
[21] K. Martins, C.E. Blenkinsopp, J. Zang, Monitoring individual wave characteristics in the inner surf with a 2-dimensional laser scanner (LiDAR), J. Sens. 2016 (2016) 1–11. http://dx.doi.org/10.1155/2016/7965431.
[22] R. Almar, R. Ibaceta, C.E. Blenkinsopp, P. Catalan, R. Cienfuegos, N. Viet, D. Thuan, D.V. UU, J.-P. Lefebvre, W. Laryea, et al., Swash-based wave energy reflection on natural beaches, in: Coastal Sediments 2015: The Proceedings of the Coastal Sediments 2015, World Scientific, 2015.
[23] K. Inch, M. Davidson, G. Masselink, P. Russell, Accurate estimation of wave reflection on a high energy, dissipative beach, J. Coast. Res. SI 75 (2016) 877–881.
[24] R. Kajima, Estimation of incident wave spectrum in the sea area influenced by reflection, in: Proceedings of Coastal Engineering in Japan, Vol. 12, 1969, pp. 9–16.
[25] E.B. Thornton, R.J. Calhoun, Spectral resolution of breakwater reflected waves, J. Waterw. Harb. Coast. Eng. Div. 98 (1972) 443–460.
[26] Y. Goda, T. Suzuki, Estimation of incident and reflected waves in random wave experiments, in: Proceedings of the 15th Conference on Coastal Engineering, Copenhagen, Denmark, 1976, pp. 828–845.
[27] E.P.D. Mansard, E.R. Funke, The measurement of incident and reflected spectra using a least squares method, in: Proceedings of the 17th Conference on Coastal Engineering, Sydney, Australia, 1980, pp. 154–172.
[28] J.A. Zelt, J.E. Skjelbreia, Estimating incident and reflected wave fields using an arbitrary number of wave gauges, in: Proceedings of the 23rd Conference on Coastal Engineering, Venice, Italy, 1992, pp. 777–789.
[29] C.-Y. Lin, C.-J. Huang, Decomposition of incident and reflected higher harmonic waves using four wave gauges, Coast. Eng. 51 (2004) 395–406. http://dx.doi.org/10.1016/j.coastaleng.2004.04.004.
[30] R.T. Guza, A.J. Bowen, Resonant interactions for waves breaking on a beach, in: Proceedings of the 15th Conference on Coastal Engineering, Honolulu, Hawaii, 1976, pp. 560–579.
[31] R. Guza, E. Thornton, R. Holman, Swash on steep and shallow beaches, in: Proceedings of the 19th Conference on Coastal Engineering, Houston, Texas, 1984, pp. 708–723.
[32] R. Almar, H. Michallet, R. Cienfuegos, P. Bonneton, M. Tissier, G. Ruessink, On the use of the radon transform in studying nearshore wave dynamics, Coast. Eng. 92 (2014) 24–30. http://dx.doi.org/10.1016/j.coastaleng.2014.06.008.
[33] R. Almar, P. Bonneton, H. Michallet, R. Cienfuegos, B.G. Ruessink, M. Tissier, On the use of the radon transform in studying wave dynamics, in: Coastal Dynamics '13: Proceedings of the Seventh Conference on Coastal Dynamics, Arcachon, France, 2013, pp. 73–82.
[34] G. Masselink, A. Ruju, D. Conley, I. Turner, G. Ruessink, A. Matias, C. Thompson, B. Castelle, J. Puleo, V. Citerone, G. Wolters, Large-scale barrier dynamics experiment II (BARDEX II): experimental design, instrumentation, test program, and data set, Coast. Eng. 113 (2016) 3–18. http://dx.doi.org/10.1016/j.coastaleng.2015.07.009.
[35] C.T. Bishop, M.A. Donelan, Measuring waves with pressure transducers, Coast. Eng. 11 (1987) 309–328. http://dx.doi.org/10.1016/0378-3839(87)90031-7.
[36] K. Inch, Surf zone hydrodynamics: Measuring waves and currents, in: Geomorphological Techniques, Chap. 3, Sec. 2.3, British Society of Geomorphology, 2014.
[37] M.O. Green, Test of sediment initial-motion theories using irregular-wave field data, Sedimentology 46 (1999) 427–441. http://dx.doi.org/10.1046/j.1365-3091.1999.00221.x.
[38] P. Nielsen, Local approximations : A new way of dealing with irregular waves, in: Proceedings of the 20th Conference on Coastal Engineering, Taipei, Taiwan, 1986, pp. 633–646.
[39] M. Townsend, J.D. Fenton, A comparison of analysis methods for wave pressure data, in: Proceedings of the 25th Conference on Coastal Engineering, Orlando, Florida, 1996, pp. 575–588.
[40] C.H. Barker, R.J. Sobey, Irregular wave kinematics from a pressure record, in: Proceedings of the 25th Conference on Coastal Engineering, Orlando, Florida, 1996, pp. 1034–1047.
[41] M.J.F. Stive, Velocity and pressure field of spilling breakers, in: Proceedings of the 17th Conference on Coastal Engineering, Sydney, Australia, 1980, pp. 547–566.
[42] I.L. Turner, P.E. Russell, T. Butt, Measurement of wave-by-wave bed-levels in the swash zone, Coast. Eng. 55 (2008) 1237–1242. http://dx.doi.org/10.1016/j.coastaleng.2008.09.009.
[43] P. Higuera, J.L. Lara, I.J. Losada, Realistic wave generation and active wave absorption for Navier-Stokes models: application to OpenFOAM®, Coast. Eng. 71 (2013) 102–118. http://dx.doi.org/10.1016/j.coastaleng.2012.07.002.
[44] N.G. Jacobsen, J. Fredsoe, J.H. Jensen, Formation and development of a breaker bar under regular waves. part 1: model description and hydrodynamics, Coast. Eng. 88 (2014) 182–193. http://dx.doi.org/10.1016/j.coastaleng.2013.12.008.
[45] R.G. Dean, R.A. Dalrymple, Water wave mechanics for engineers and scientists, Advanced Series on Ocean Engineering: Volume 2, World Scientific, 1991.
[46] E. Berberović, N.P. van Hinsberg, S. Jakirlić, I.V. Roisman, C. Tropea, Drop impact onto a liquid layer of finite thickness:dynamics of the cavity evolution, Phys. Rev. E 79 (2009) 036306. http://dx.doi.org/10.1103/PhysRevE.79.036306.
[47] F.R. Menter, Two-equation eddy-viscosity turbulence models for engineering applications, AIAA J. 32 (1994) 1598–1605. http://dx.doi.org/10.2514/3.12149.
[48] S.A. Brown, V. Magar, D.M. Greaves, D.C. Conley, An evaluation of rans turbulence closure models for spilling breakers, in: Proceedings of the 34th Conference on Coastal Engineering, Seoul, Korea, 2014.
[49] J.Z. Gailani, S.J. Smith, Sediment Transport Analysis from OBS/EMCM During Storms, Technical Report, DTIC Document, 2000.
[50] S. Elgar, B. Raubenheimer, R.T. Guza, Quality control of acoustic doppler velocimeter data in the surfzone, Meas. Sci. Technol. 16 (2005) 1889. http://dx.doi.org/10.1088/0957-0233/16/10/002.
[51] Z.-C. Huang, K.-S. Hwang, Measurements of surface thermal structure, kinematics, and turbulence of a large-scale solitary breaking wave using infrared imaging techniques, Coast. Eng. 96 (2015) 132–147. http://dx.doi.org/10.1016/j.coastaleng.2014.12.005.
[52] C.E. Blenkinsopp, J.R. Chaplin, Void fraction measurements and scale effects in breaking waves in freshwater and seawater, Coast. Eng. 58 (2011) 417–428. http://dx.doi.org/10.1016/j.coastaleng.2010.12.006.
[53] B. Hofland, E. Diamantidou, P. van Steeg, P. Meys, Wave runup and wave overtopping measurements using a laser scanner, Coast. Eng. 106 (2015) 20–29. http://dx.doi.org/10.1016/j.coastaleng.2015.09.003.
[54] J. Radon, Über die bestimmung von funktionen durch ihre integralwerte längs gewisser mannigfaltigkeiten, Akad. Wiss. 69 (1917) 262–277.
[55] J.R. Miles, P.E. Russell, D.A. Huntley, Sediment transport and wave reflection near a seawall, in: Proceedings of the 25th Conference on Coastal Engineering, Orlando,

Florida, 1996, pp. 2612–2624.
[56] H.E. Power, M.G. Hughes, T. Aagaard, T.E. Baldock, Nearshore wave height variation in unsaturated surf, J. Geophys. Res.: Ocean. 115 (2010). http://dx.doi.org/10.1029/2009JC005758.
[57] H.E. Power, M.G. Hughes, T.E. Baldock, A novel method for tracking individual waves in the surf zone, Coast. Eng. 98 (2015) 26–30. http://dx.doi.org/10.1016/j.coastaleng.2015.01.006.
[58] M. Postacchini, M. Brocchini, A wave-by-wave analysis for the evaluation of the breaking-wave celerity, Appl. Ocean Res. 46 (2014) 15–27. http://dx.doi.org/10.1016/j.apor.2014.01.005.
[59] G.C.J. Morgan, J. Zang, D. Greaves, A. Heath, C. Whitlow, J. Young, Using the rasInterFoam CFD model for wave transformation and coastal modelling, in: Proceedings of the 32nd Conference on Coastal Engineering, Shanghai, China, 2010.
[60] L.P. Almeida, G. Masselink, P.E. Russell, M.A. Davidson, Observations of gravel beach dynamics during high energy wave conditions using a laser scanner, Geomorphology 228 (2015) 15–27. http://dx.doi.org/10.1016/j.geomorph.2014.08.019.
[61] A. Baquerizo, M.A. Losada, J.M. Smith, Wave reflection from beaches:a predictive model, J. Coast. Res. 14 (1998) 291–298.
[62] I.J. Mario-Tapia, P.E. Russell, T.J. O'Hare, M.A. Davidson, D.A. Huntley, Cross-shore sediment transport on natural beaches and its relation to sandbar migration patterns:1. field observations and derivation of a transport parameterization, J. Geophys. Res.: Ocean. 112 (2007). http://dx.doi.org/10.1029/2005JC002893.
[63] B. Robertson, K. Hall, Z. Richard, I. Nistor, Breaking waves:review of characteristic relationships, Coast. Eng. J. 55 (2013) 1350002. http://dx.doi.org/10.1142/S0578563413500022.
[64] U. Putrevu, I.A. Svendsen, Vertical structure of the undertow outside the surf zone, J. Geophys. Res.: Ocean. 98 (1993) 22707–22716. http://dx.doi.org/10.1029/93JC02399.
[65] F.J. Mendez, I.J. Losada, R.A. Dalrymple, M.A. Losada, Effects of wave reflection and dissipation on wave-induced second order magnitudes, in: Proceedings of the 26th Conference on Coastal Engineering, Copenhagen, Denmark, 1998, pp. 537–500.
[66] M. Dyhr-Nielson, T. Sørensen, Some sand transport phenomena on coasts with bars, in: Proceedings of the 12th Conference on Coastal Engineering, Washington, D.C., 1970, pp. 855–865.
[67] E.B. Thornton, R.T. Humiston, W. Birkemeier, Bar/trough generation on a natural beach, J. Geophys. Res.: Ocean. 101 (1996) 12097–12110. http://dx.doi.org/10.1029/96JC00209.
[68] J. Fredsœ, R. Deigaard, Mechanics of coastal sediment transport, Advanced Series on Ocean Engineering: Volume 3, World Scientific, 1992.
[69] S. Elgar, E.L. Gallagher, R.T. Guza, Nearshore sandbar migration, J. Geophys. Res.: Ocean. 106 (2001) 11623–11627. http://dx.doi.org/10.1029/2000JC000389.
[70] P.A. Silva, T. Abreu, D.A. van der A, F. Sancho, B.G. Ruessink, J. van der Werf, J.S. Ribberink, Sediment transport in nonlinear skewed oscillatory flows: Transkew experiments, Journal of Hydraulic Research, 49, 2011, 72–80. http://dx.doi.org/10.1080/00221686.2011.592681.
[71] F. Grasso, H. Michallet, E. Barthlemy, Sediment transport associated with morphological beach changes forced by irregular asymmetric, skewed waves, J. Geophys. Res.: Ocean. 116 (2011) c03020. http://dx.doi.org/10.1029/2010JC006550.
[72] A.J. Bowen, Simple models of nearshore sedimentation, beach profiles and longshore bars, The Coastline of Canada, Geological Survey of Canada, 1980, 1–11.
[73] A.M. Bernabeu, R. Medina, C. Vidal, Wave reflection on natural beaches: an equilibrium beach profile model, Estuar., Coast. Shelf Sci. 57 (2003) 577–585. http://dx.doi.org/10.1016/S0272-7714(02)00393-1.
[74] E. Sánchez-Badorrey, M.A. Losada, J. Rodero, Sediment transport patterns in front of reflective structures under wind wave-dominated conditions, Coast. Eng. 55 (2008) 685–700. http://dx.doi.org/10.1016/j.coastaleng.2007.11.005.
[75] J.M. Alsina, I. Cáceres, M. Brocchini, T.E. Baldock, An experimental study on sediment transport and bed evolution under different swash zone morphological conditions, Coast. Eng. 68 (2012) 31–43. http://dx.doi.org/10.1016/j.coastaleng.2012.04.008.
[76] A. Torres-Freyermuth, J.L. Lara, I.J. Losada, Numerical modelling of short- and long-wave transformation on a barred beach, Coast. Eng. 57 (2010) 317–330. http://dx.doi.org/10.1016/j.coastaleng.2009.10.013.